Available online at www.sciencedirect.com
SCIENCE DIRECT®
Journal of Computational Physics 190 (2003) 64–99
JOURNAL OF COMPUTATIONAL PHYSICS
www.elsevier.com/locate/jcp

Numerical boundary conditions for sound scattering simulation

R. Berthet [a,*], D. Astruc [b]

[a] *Laboratoire de Physique Statistique, UMR CNRS 8550, École Normale Supérieure, 24 rue Lhomond, 75231 Paris Cedex 05, France*
[b] *Institut de Mécanique des Fluides de Toulouse, UMR 5502 CNRS/INP-UPS, Allée du Pr. Soula, 31400 Toulouse, France*

Received 24 June 2002; received in revised form 23 April 2003; accepted 30 April 2003

Abstract

A hierarchy of boundary algorithms based both on a decomposition of the flow field and on a characteristic formulation of the conservation equations is introduced for the computation of sound wave scattering by vortical flows. The robustness of the proposed algorithms is analysed. Sound and vorticity wave reflexion at an open boundary are estimated for various mean flows and different sound wave fields. A direct assessment of this algorithm coupled with an interior 2–4 Mac Cormack scheme for sound scattering computations based on the 2D inviscid gas dynamics equations is performed using comparison with theoretical scattering results.

1. Introduction

Sound scattering phenomenon arises from the weakly non-linear interaction between the acoustic and vortical modes of a compressible flow, which generate an additional acoustic mode [1]. This coupling is relevant in the problem of sound propagation in turbulent compressible flows [2] and may be used as a probing technique in experimental investigation of turbulent flows [3]. Despite a lot of experimental [4–9] and theoretical [10–12] works performed over the last 20 years, the influence of the turbulent mean flow on the sound propagation and sound-mean flows interactions are still open topics.

A simple sound scattering setup is shown on Fig. 1: a linear incident plane wave (sound pressure p_i, wavenumber $k = 2\pi/\lambda$, celerity c, frequency $\nu = \lambda/c$ and pressure amplitude p_{0i})

$$p_i = p_{0i}\Re[e^{i(2\pi\nu t - kx)}], \tag{1}$$

where ($\Re[z]$ is the real part of the complex number z) is emitted at the western side of the computational domain and it interacts with a mean vortical flow (typical size L, typical velocity U, Mach number

* Corresponding author.
E-mail address: rberthet@lps.ens.fr (R. Berthet).

0021-9991/$ - see front matter
doi:10.1016/S0021-9991(03)00254-7

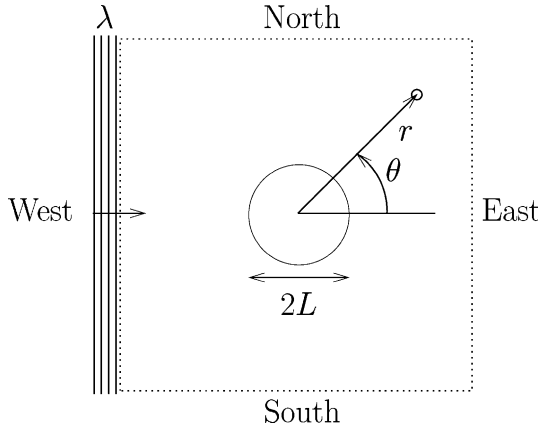

Fig. 1. Schematic configuration for sound scattering computations. The computational domain is limited by the dashed box.

$\mathscr{M} = U/c$). In real experiments, sound-mean flow interactions are analysed at several points (r, θ) of the domain, where the sound wave pressure p_s is recorded [4,5,7–9,13]. The scattering process is usually characterized by two physical quantities [14]: the scattered wave pressure p_{scat}, computed from p_s and p_i,

$$p_{scat} = p_s - p_i \tag{2}$$

and the scattered amplitude $f(\theta)$, defined in the far-field regime ($r \gg 2\pi L^2/\lambda$)

$$\frac{p_{scat}}{p_{0i}} = \Re\left[f(\theta)\frac{e^{ikr}}{\sqrt{r}}\right] \tag{3}$$

in two dimensions.

Numerical computation proved to be a powerful and accurate tool to investigate sound-mean flow interactions occurring in aeroacoustics problems. Various level of approximation can be used for this purpose: direct [13,15–19] or large-eddy numerical simulation [20] of the gas dynamics equations, splitting of the Euler equations into an incompressible flow and a fluctuating part [21], numerical simulation of the linearized acoustic field around the mean flow [22], computation of the parabolic approximation for the sound propagation through the mean flow [23,24]. However, very few numerical works are related to the sound scattering problem. The only work based on a direct numerical simulation of the flow conservation equation has been performed by Colonius et al. [15] who studied the scattering of a plane sound wave by a single vortex. As pointed out by Colonius et al. [15], such a study is made very difficult because: (i) several spatial scales – i.e. characteristic size of the mean flow and wavelength of the sound waves – must be considered together; (ii) the different physical phenomenons amplitudes range over several orders of magnitude – the scattered wave amplitude is usually one or two orders of magnitude smaller than the incident sound wave amplitude which is itself four orders of magnitude smaller than the mean flow. Thus, when designing a numerical model for sound scattering computations, the interior discretization scheme has to be chosen with care to ensure high quality dispersion and low damping properties. In addition, a proper open boundary algorithm is needed to avoid as much as possible: (i) the parasitic reflection of outgoing sound waves at the computational domain boundaries; (ii) the sound wave generation by outgoing vorticity waves.

A vast body of literature deals with the open boundary conditions problem for compressible flows computations [25–32]. In a review paper, Givoli [33] discusses possible local and non-local boundary conditions. Amongst these techniques, a classical way to impose non-reflecting conditions is to cancel the

incoming characteristic waves amplitude, following Thompson [34]. Although efficient in limiting spurious reflections, this technique leads to an ill posed problem as no value for the external pressure is provided by an incoming acoustic wave. Some improvements have been proposed [27,35], where informations on the pressure value at infinity is provided. However, the boundary algorithm becomes weakly reflecting and does not allow an accurate modelling of physical situations like scattering problems. Colonius et al. [29] have used an algorithm which model non-reflecting boundaries in the presence of a mean flow to perform sound scattering studies. The objective of this work is to design a boundary algorithm for numerical studies of sound scattering based on the direct simulation of conservation equations. This boundary algorithm should be efficient even if the mean flow vorticity does not vanish at the computational domain boundaries and for a wide range of physical parameters i.e. $\mathscr{M}$, λ/L, p_{0_i}/p_{ref}. Starting from a decomposition of the flow into a steady component and a fluctuation, a new set of three approximate conservation equations which are solved in a characteristic form at the boundary of the computational domain is introduced. One of them is the approximation used by Colonius et al. [29]. The validity conditions of these approximations are given and the robustness of these techniques is investigated numerically with respect to the mean flow type. The sound wave generation by outgoing vorticity wave is investigated. Then, a complete analysis of plane and cylindrical sound wave reflection at an open boundary is performed. In real sound-scattering configurations, the computational results are compared to analytical results in order to validate the boundary algorithm for such problems.

The paper is organized as follows: the numerical algorithm is described in the following section for the interior scheme and in Section 3 for the boundary algorithm. Section 4 is dedicated to general purpose tests: the boundary algorithm stability is analysed and the parasitic boundary reflections are quantified. The efficiency of the boundary algorithm for scattering modelling is illustrated in Section 5 before the conclusion.

2. Numerical algorithm

The numerical model solves the conservation equations governing the time evolution of a compressible and isentropic flow in a two-dimensional (2D) domain:

$$\frac{\partial U}{\partial t}+\frac{\partial F}{\partial x}+\frac{\partial G}{\partial y}=0, \tag{4}$$

where

$$U=\begin{pmatrix}\rho\\ \rho u\\ \rho v\\ E\end{pmatrix} \tag{5}$$

are the conservative variables. The inviscid fluxes are given by:

$$F=\begin{pmatrix}\rho u\\ \rho u^2+p\\ \rho vu\\ (E+p)u\end{pmatrix},\quad G=\begin{pmatrix}\rho v\\ \rho uv\\ \rho v^2+p\\ (E+p)v\end{pmatrix}, \tag{6}$$

where ρ, u, v, E and p denote, respectively, the density, the velocity components along x and y directions, the total energy (kinetic energy and internal energy) per unit of volume and the pressure. Assuming a perfect gas,

$$p = (\gamma - 1)\left(E - \frac{1}{2}\rho(u^2 + v^2)\right), \tag{7}$$

where $\gamma = C_p/C_v$ is the ratio of isobaric and isochoric specific heat capacities, $\gamma = 1.4$ for air at standard temperature and pressure conditions. Please note that the energy conservation is used during the numerical computations instead of the Laplace equation (valid for any isentropic transformation of a perfect gas)

$$\frac{p}{\rho^{\gamma}} = C^{\text{te}} \tag{8}$$

to limit numerical errors. The interior scheme is based on an enhanced version of the Mac Cormack scheme. Based on a predictor–corrector technique, this scheme is second-order accurate in time and fourth order accurate in space. Details about the numerical algorithm can be found in Turkel [36] and in Gamet and Estivalèzes [37].

3. Boundary algorithm

3.1. Introduction

A large amount of methods have been developed in the recent years to compute accurate non-reflective boundary conditions (see for example [38,39]). They can be roughly decomposed into non-local and local methods. Non-local methods usually involves integral relations at the boundary [40,41] or Fourier transform of the physical quantities [42,43]. They can be non-local in time (the temporal evolution of a boundary point is related to its past behavior, which implies some memory effects at the boundary), non-local in space (a point at the boundary interacts with its neighborhood and with any other point of the boundary) or non-local both in time and space. All these methods are exact boundary conditions but they are cumbersome and computationally expensive (a large amount of data storage is required). Approximate local boundary conditions can be used instead. Different approximation techniques can be used: asymptotic expansions of the wave equation (radiation boundary conditions [25,44–46]), characteristics based methods (analysis of the physical boundary in terms of characteristics waves crossing the boundary [27,43,47]), buffer zone (the computational domain is surrounded by a zone, where some damping is added to cancel any reflective wave. This damping can be directly introduced in the basic governing equations [19,48] or can be numerically introduced by a grid stretching [19,29,48]) or perfectly matched layer (PML) (the computational domain is surrounded by a zone, where the waves are absorbed [19,49]). Some filtering techniques may be introduced to avoid spurious reflections resulting from the above boundary treatments [50].

All these boundary treatments have their own advantages and drawbacks: buffer zone techniques are inefficient when a given boundary involves both inflow and outflow regions, asymptotic expansions and PML methods can only be applied to linear systems, whereas characteristics based methods often become inaccurate for large wave amplitudes [51]. Amongst all these techniques, the choice of a boundary algorithm for aeroacoustics computations also depends on the physical problem to solve. For sound-mean flow interactions in various physical setups, non-reflective inflow/outflow boundaries have to be designed. Moreover, to deeply analyse the sound-mean flow interactions, we want to compute the full non-linear aeroacoustic problem model by Eq. (4). Thus, a Thompson's like approach [34] based on a characteristics analysis of the boundary is chosen.

3.2. Theoretical framework

In order to compute sound scattering simulations, Colonius et al. [29] proposed a method to impose non-reflecting boundary conditions in the presence of a mean flow. Linearizing the global flow with respect to a

steady mean flow and neglecting high order terms, they deduced a partial differential equation for the first-order perturbation term. This equation is solved using a characteristic method. A detailed analysis of this boundary algorithm is performed in various practical situations [29]. When the mean flow is not close to an spatially uniform mean flow, this boundary treatment produces a large acoustic reflected wave [29]. We present here some improvements of this method suitable for mean flows which have a non-trivial topology at a given boundary: a hierarchy of implementations to solve the boundary conditions problem with a characteristic formulation is discussed and the range of validity of these new implementations is analysed.

At each time step n and at each boundary point (i,j), a linear decomposition of the solution $V(t)$ (primitive variables $(\rho u v p)^t$) is performed with respect to an arbitrary reference mean flow V_0, assumed to be steady in the frame of reference of the computation:

$$V(n,i,j) = V_0(i,j) + V'(n,i,j), \tag{9}$$

where

$$V = \begin{pmatrix} \rho \\ u \\ v \\ p \end{pmatrix}, \quad V_0 = \begin{pmatrix} \rho_0 \\ u_0 \\ v_0 \\ p_0 \end{pmatrix}, \quad V' = \begin{pmatrix} \rho' \\ u' \\ v' \\ p' \end{pmatrix}. \tag{10}$$

Eq. (9) corresponds to the decomposition of the flow field into a mean steady flow V_0 and a fluctuating part V'. $V_0(i,j)$ is a reference steady mean flow which may differ from a solution of the inviscid flow Eq. (4): $V_0(i,j)$ can be an incompressible mean flow or the initial flow field of the numerical simulation. $V'(n,i,j)$ is the fluctuating part with respect to the mean flow (mean flow perturbations). The temporal evolution of V' includes two different mechanisms. First, it includes sound waves propagating in the computational domain and the unsteadiness of the physical mean flow. Second, $V_0(i,j)$ a priori differs from the physical compressible mean flow at time step n and may induced numerical perturbations which are also taken into account in $V'(n,i,j)$.

$V'(n,i,j)$ can be split into

$$V'(n,i,j) = \widehat{V}(n,i,j) - V_{\text{ref}}, \tag{11}$$

where

$$\widehat{V} = \begin{pmatrix} \hat{\rho} \\ \hat{u} \\ \hat{v}, \\ \hat{p} \end{pmatrix}, \quad V_{\text{ref}} = \begin{pmatrix} \rho_{\text{ref}} \\ 0 \\ 0 \\ p_{\text{ref}} \end{pmatrix}. \tag{12}$$

Eq. (11) introduces a reference state V_{ref} for a fluid at rest (e.g., standard values of air density and pressure). It should be noted that the temporal evolution of $\widehat{V}$ and V' are the same.

In the following, the temporal index n and the spatial indexes (i,j) are dropped. Eq. (4) can be recast in terms of the primitive variables V:

$$\frac{\partial V}{\partial t} + A\frac{\partial V}{\partial x} + B\frac{\partial V}{\partial y} = 0 \tag{13}$$

with

$$A = \begin{pmatrix} u & \rho & 0 & 0 \\ 0 & u & 0 & 1/\rho \\ 0 & 0 & u & 0 \\ 0 & \gamma p & 0 & u \end{pmatrix}, \quad B = \begin{pmatrix} v & 0 & \rho & 0 \\ 0 & v & 0 & 0 \\ 0 & 0 & v & 1/\rho \\ 0 & 0 & \gamma p & v \end{pmatrix}. \tag{14}$$

Using the fact that V_0 is a steady solution of Eq. (13) and only assuming small density fluctuations $\rho' \ll \rho_0$,

$$\frac{1}{\rho} \simeq \frac{1}{\rho_0} - \frac{\rho'}{\rho_0^2}. \tag{15}$$

Eq. (13) reads:

$$\frac{\partial \widehat{V}}{\partial t} + (A_0 + A')\frac{\partial \widehat{V}}{\partial x} + (B_0 + B')\frac{\partial \widehat{V}}{\partial y} + A'\frac{\partial V_0}{\partial x} + B'\frac{\partial V_0}{\partial y} = 0 \tag{16}$$

with

$$A_0 = \begin{pmatrix} u_0 & \rho_0 & 0 & 0 \\ 0 & u_0 & 0 & 1/\rho_0 \\ 0 & 0 & u_0 & 0 \\ 0 & \gamma p_0 & 0 & u_0 \end{pmatrix}, \quad B_0 = \begin{pmatrix} v_0 & 0 & \rho_0 & 0 \\ 0 & v_0 & 0 & 0 \\ 0 & 0 & v_0 & 1/\rho_0 \\ 0 & 0 & \gamma p_0 & v_0 \end{pmatrix}, \tag{17}$$

and

$$A' = \begin{pmatrix} u' & \rho' & 0 & 0 \\ 0 & u' & 0 & -\rho'/\rho_0^2 \\ 0 & 0 & u' & 0 \\ 0 & \gamma p' & 0 & u' \end{pmatrix}, \quad B' = \begin{pmatrix} v' & 0 & \rho' & 0 \\ 0 & v' & 0 & 0 \\ 0 & 0 & v' & -\rho'/\rho_0^2 \\ 0 & 0 & \gamma p' & v' \end{pmatrix}. \tag{18}$$

The two last terms of Eq. (16) can be recasted into

$$A'\frac{\partial V_0}{\partial x} + B'\frac{\partial V_0}{\partial y} = C_0 V' \tag{19}$$

with

$$C_0 = \begin{pmatrix} \left(\dfrac{\partial u_0}{\partial x} + \dfrac{\partial v_0}{\partial y}\right) & \dfrac{\partial \rho_0}{\partial x} & \dfrac{\partial \rho_0}{\partial y} & 0 \\ \dfrac{-1}{\rho_0^2}\dfrac{\partial p_0}{\partial x} & \dfrac{\partial u_0}{\partial x} & \dfrac{\partial u_0}{\partial y} & 0 \\ \dfrac{-1}{\rho_0^2}\dfrac{\partial p_0}{\partial y} & \dfrac{\partial v_0}{\partial x} & \dfrac{\partial v_0}{\partial y} & 0 \\ 0 & \dfrac{\partial p_0}{\partial x} & \dfrac{\partial p_0}{\partial y} & \gamma\left(\dfrac{\partial u_0}{\partial x} + \dfrac{\partial v_0}{\partial y}\right) \end{pmatrix}, \tag{20}$$

which leads to

$$\frac{\partial \widehat{V}}{\partial t} + (A_0 + A')\frac{\partial \widehat{V}}{\partial x} + (B_0 + B')\frac{\partial \widehat{V}}{\partial y} + C_0 V' = 0. \tag{21}$$

Please note that a small density perturbation $\rho' \ll \rho_0$ and a steady mean flow V_0 are the only required assumptions at this stage.

In order to use the characteristic method [26,27], we have to neglect the last term of (21)

$$\frac{\partial \widehat{V}}{\partial t} + (A_0 + A')\frac{\partial \widehat{V}}{\partial x} + (B_0 + B')\frac{\partial \widehat{V}}{\partial y} \simeq 0. \tag{22}$$

Then, Eq. (22) has a structure similar to the one derived from a linear analysis of Eq. (4) [26]. This approximation is valid if $C_0 V'$ can be neglected in front of $(A_0 + A')\frac{\partial \widehat{V}}{\partial x}$ and $(B_0 + B')\frac{\partial \widehat{V}}{\partial y}$. Setting Λ' the typical

scale of the perturbation V', X' its typical amplitude, l_0 the typical scale of the reference mean flow V_0 at the boundary, X_0 its amplitude and $X = X_0 + X'$ the amplitude of V, we can deduced from Eq. (19) that

$$C_0 V' \simeq \frac{X_0}{l_0} X' \tag{23}$$

and from Eq. (17) that

$$(A_0 + A')\frac{\partial \widehat{V}}{\partial x} = (A_0 + A')\frac{\partial V'}{\partial x} \simeq \left(X_0 + X'\right)\frac{X'}{\Lambda'} = X\frac{X'}{\Lambda'}. \tag{24}$$

Thus, neglecting $C_0 V'$ in front of $(A_0 + A')\frac{\widehat{\partial V}}{\partial x}$ leads to the condition

$$\frac{X_0}{l_0} \ll \frac{X}{\Lambda'}. \tag{25}$$

As pointed out before, Λ' may be different from the sound wavelength λ (the perturbation V' may be different from physical acoustic phenomenons because the mean flow may be unsteady or the reference mean flow V_0 may be incompressible). Moreover, l_0 is the typical scale of the mean flow gradients at the boundaries, which is different from the mean flow size L (e.g., Eq. (48)). Condition (25) must be satisfied to ensure the validity of the boundary conditions procedure. Thus, large computational domains may be required depending on the mean flow structure.

In order to analyse Eq. (25), let us recast it

$$\frac{X_0}{l_0}\left(1 - \frac{l_0}{\Lambda'}\right) \ll \frac{X'}{\Lambda'}. \tag{26}$$

The right-hand side corresponds to the perturbation gradients, whereas the left-hand side takes into account the reference mean flow gradients and the relative perturbation scale Λ'/l_0. Thus, the reference mean flow gradients must be small compared with the perturbation gradients, according to a non-trivial condition on the relative perturbation scale Λ'/l_0. Thus, the physical flow V may be different from the reference mean flow V_0 without breaking down condition (25) (see Section 4.2).

Starting from the above decomposition, three different ways for the numerical implementation of the algorithm are possible:

I_1: full computation of Eq. (22):

$$\frac{\partial \widehat{V}}{\partial t} + \underbrace{(A_0 + A')}_{\mathscr{A}_1}\frac{\partial \widehat{V}}{\partial x} + \underbrace{(B_0 + B')}_{\mathscr{B}_1}\frac{\partial \widehat{V}}{\partial y} = 0. \tag{27}$$

Then, the physical fields on the boundaries have only to satisfy

$$X_0/l_0 \ll X/\Lambda' \quad \text{and} \quad \rho' \ll \rho_0, \tag{28}$$

I_2: first-order linearization of Eq. (22), which leads to

$$\frac{\partial \widehat{V}}{\partial t} + \underbrace{A_0}_{\mathscr{A}_2}\frac{\partial \widehat{V}}{\partial x} + \underbrace{B_0}_{\mathscr{B}_2}\frac{\partial \widehat{V}}{\partial y} = 0. \tag{29}$$

This implementation corresponds to the linear decomposition around the mean flow used by Colonius et al. [29]: A' is neglected in comparison with A_0, which means that $V' \ll V_0$. This implies that the flow V remains close to the reference mean flow V_0 during the computation. The validity range of this implementation is limited by the conditions: $V' \ll V_0$ and Eq. (25) which reads

$$\Lambda' \ll l_0. \tag{30}$$

If the reference mean flow V_0 is uniform at the boundary, $l_0 \to \infty$ and Eq. (30) is always satisfied. In this case, $V' \ll V_0$ remains the only required assumption for this implementation [29].

I_3: decomposition of A' and B' with respect to the reference state:

$$A' = \widehat{A}_0 - A_{\text{ref}}, \quad B' = \widehat{B}_0 - B_{\text{ref}} \tag{31}$$

with

$$\widehat{A}_0 = \begin{pmatrix} \hat{u} & \hat{\rho} & 0 & 0 \\ 0 & \hat{u} & 0 & -\hat{\rho}/\rho_0^2 \\ 0 & 0 & \hat{u} & 0 \\ 0 & \gamma\hat{p} & 0 & \hat{u} \end{pmatrix}, \quad A_{\text{ref}} = \begin{pmatrix} 0 & \rho_{\text{ref}} & 0 & 0 \\ 0 & 0 & 0 & -\rho_{\text{ref}}/\rho_0^2 \\ 0 & 0 & 0 & 0 \\ 0 & \gamma p_{\text{ref}} & 0 & 0 \end{pmatrix} \tag{32}$$

and

$$\widehat{B}_0 = \begin{pmatrix} \hat{v} & \hat{\rho} & 0 & 0 \\ 0 & \hat{v} & 0 & 0 \\ 0 & 0 & \hat{v} & -\hat{\rho}/\rho_0^2 \\ 0 & 0 & \gamma\hat{p} & \hat{v} \end{pmatrix}, \quad B_{\text{ref}} = \begin{pmatrix} 0 & 0 & \rho_{\text{ref}} & 0 \\ 0 & 0 & 0 & 0 \\ 0 & 0 & 0 & -\rho_{\text{ref}}/\rho_0^2 \\ 0 & 0 & \gamma p_{\text{ref}} & 0 \end{pmatrix}. \tag{33}$$

Let us consider a boundary, where the perturbation V' is small compared to the mean flow V_0 and suppose that V_0 remains close to the fluid at rest

$$V' \ll V_0 \quad \text{and} \quad V_0 \simeq V_{\text{ref}}. \tag{34}$$

Then

$$\hat{\rho} = \rho' + \rho_{\text{ref}} \simeq \rho_{\text{ref}} \simeq \rho_0 \gg \rho', \tag{35}$$

which leads to

$$\widehat{A}_0 \simeq \widehat{A} = \begin{pmatrix} \hat{u} & \hat{\rho} & 0 & 0 \\ 0 & \hat{u} & 0 & -\hat{\rho}/\hat{\rho}^2 \\ 0 & 0 & \hat{u} & 0 \\ 0 & \gamma\hat{p} & 0 & \hat{u} \end{pmatrix} \quad \text{and} \quad \widehat{B}_0 \simeq \widehat{B}. \tag{36}$$

Thus, $A_0 + A' = A_0 + \widehat{A}_0 - A_{\text{ref}} \simeq \widehat{A}_0 \simeq \widehat{A}$. Eq. (22) can be approximated by

$$\frac{\partial \widehat{V}}{\partial t} + \underbrace{\widehat{A}}_{\mathscr{A}_3} \frac{\partial \widehat{V}}{\partial x} + \underbrace{\widehat{B}}_{\mathscr{B}_3} \frac{\partial \widehat{V}}{\partial y} = 0, \tag{37}$$

which has to be solved at the boundary.

For small perturbations $V' \ll V_0$, if the mean flow is at rest at the boundary, implementation I_3 is identical to implementation I_2: $A_0 = A_{\text{ref}}$ and $A_0 + A' = \widehat{A}_0$. I_2 being deduced from I_1 when $V' \ll V_0$, I_3 is also equivalent to I_1 in this case. Moreover, implementation I_3 is similar to implementation I_1 for small perturbations U': in this case, $A_0 \gg A'$.

Implementations I_1 (Eq. (27)), I_2 (Eq. (29)) or I_2 (Eq. (37)) are the basis of the proposed numerical boundary algorithms. They require the choice of a reference steady mean flow, the condition $\rho' \ll \rho_0$ and the following assumptions:

$$\begin{aligned} &I_1 : V_0/l_0 \ll V/\Lambda' \text{ near the boundary,} \\ &I_2 : V' \ll V_0 \text{ and } \Lambda' \ll l_0 \text{ near the boundary,} \\ &I_3 : V' \ll V_0,\ \Lambda' \ll l_0 \text{ and } V_0 \simeq V_{\text{ref}} \text{ near the boundary,} \end{aligned} \tag{38}$$

where Λ' is the typical wavelength of the perturbation V' and l_0 is the typical scale of the mean flow V_0 at the boundary.

3.3. Numerical resolution

The perturbated field $\widehat{V}$ is advanced in time at a given boundary using one of the three implementations I_1, I_2 or I_3, i.e. solving Eqs. (27), (29) or (37). This resolution is based on a Thompson-like approach [26] using a characteristic method. For a boundary located at $x = x_0$ ($x > x_0$ corresponding to the exterior of the computational domain), the one-dimensional (1D) characteristic analysis of Eqs. (27), (29) or (37) normal to the boundary leads to four characteristic variables W_i [34]

$$\begin{array}{ll} W_1 = \hat{p} - c_I^2 \hat{\rho} & \text{entropy mode,} \\ W_2 = \hat{v} & \text{advection mode,} \\ W_3 = \hat{p} + \rho_I c_I \hat{u} & \text{sound mode,} \\ W_4 = \hat{p} - \rho_I c_I \hat{u} & \text{sound mode} \end{array} \tag{39}$$

corresponding to the four eigenvalues $\lambda_1 = u_I = \lambda_2$, $\lambda_3 = u_I + c_I$ and $\lambda_4 = u_I - c_I$, c_I being the local sound speed. The quantities indexed by I_i are computed from matrix $\mathscr{A}_i$, according to the given implementation I_i. A temporal approach or a spatial approach are both possible to solve the boundary conditions problem for a given interior scheme [28]. The characteristic variables temporal evolution is given by:

$$\begin{cases} w_1 = \dfrac{\partial W_1}{\partial t} = \dfrac{\partial \hat{p}}{\partial t} - c_I^2 \dfrac{\partial \hat{\rho}}{\partial t}, \\ w_2 = \dfrac{\partial W_2}{\partial t} = \dfrac{\partial \hat{v}}{\partial t}, \\ w_3 = \dfrac{\partial W_3}{\partial t} = \dfrac{\partial \hat{p}}{\partial t} + \rho_I c_I \dfrac{\partial \hat{u}}{\partial t}, \\ w_4 = \dfrac{\partial W_4}{\partial t} = \dfrac{\partial \hat{p}}{\partial t} - \rho_I c_I \dfrac{\partial \hat{u}}{\partial t}, \end{cases} \tag{40}$$

whereas the spatial evolution is given by:

$$\begin{aligned} \frac{\partial W_1}{\partial x} &= \frac{\partial \hat{p}}{\partial x} - c_I^2 \frac{\partial \hat{\rho}}{\partial x}, \\ \frac{\partial W_2}{\partial x} &= \frac{\partial \hat{v}}{\partial x}, \\ \frac{\partial W_3}{\partial x} &= \frac{\partial \hat{p}}{\partial x} + \rho_I c_I \frac{\partial \hat{u}}{\partial x}, \\ \frac{\partial W_4}{\partial x} &= \frac{\partial \hat{p}}{\partial x} - \rho_I c_I \frac{\partial \hat{u}}{\partial x}. \end{aligned} \tag{41}$$

It should be noted that both approaches are strictly equivalent for a 1D scheme [47]. Together with the Mac Cormack interior scheme, we use a flux extrapolation procedure and the temporal approach (40), following Hayder and Turkel [50]: the boundary problem is solved using Eq. (40) to advance $\widehat{V}$ in time from n to $n + 1$. Then, the conservative variables (5) are rebuilt at step $n + 1$ using relations (9) and (11). This last step completes the boundary conditions treatment. A similar method can be developed for a boundary located at $y = y_0$.

3.4. Boundary conditions for sound scattering computations

In sound scattering by subsonic flows studies, two types of boundary conditions are needed (see Fig. 1): open non-reflecting boundary and non-reflecting sound emitter to model a sound transducer. From their expected behavior, it is possible to derive the values of w_i's for each boundary condition:

- open non-reflecting boundary condition: no reflection at the boundary, i.e. no incoming wave in the domain, is expected. If the boundary is a subsonic inlet, $w_1 = w_2 = w_4 = 0$ is imposed and w_3 is computed from the interior values, whereas for a subsonic outlet $w_4 = 0$ is imposed, w_1, w_2 and w_3 are computed from interior values;
- non-reflecting plane wave emitter: the sound wave velocity is imposed on the boundary:

$$\begin{cases} u_s = u_{0_s} \sin(2\pi\nu t), \\ v_s = 0 \end{cases} \tag{42}$$

with $\nu = c/\lambda$ the sound frequency and u_{0_s} the sound emitter amplitude. In addition, this emitter should be non-reflecting, i.e. the only incoming wave is the emitted sound wave. In terms of characteristic variables, the velocity components of $\widehat{V}$ can be written:

$$\begin{cases} \dfrac{\partial \hat{u}}{\partial t} = \dfrac{1}{2\rho c}[w_3 - w_4], \\ \dfrac{\partial \hat{v}}{\partial t} = w_2. \end{cases} \tag{43}$$

Thus, for an inlet boundary

$$w_1 = w_2 = 0 \quad \text{and} \quad w_4 = -2\rho c \frac{\partial u_s}{\partial t} \tag{44}$$

and for an outlet boundary

$$w_4 = -2\rho c \frac{\partial u_s}{\partial t}. \tag{45}$$

As only the time derivative of the incoming sound wave is imposed, a non-zero mean value may occur. In all our numerical computations, this mean value proved to be at least one order of magnitude smaller than the amplitude of the incoming sound wave. Thus, it neither influences the oscillating physical fields nor the mean flow fields.

4. Boundary implementation evaluation

In this section, we focus on tests performed to check the practical relevance of the three different implementations of the numerical boundary algorithm. Following Chu and Kovásznay [1], the evolution of a compressible flow can be analysed in terms of non-linear interactions between three modes: a vorticity mode, a sound mode and an entropy mode. We deal with isentropic flows. Thus, the vorticity mode and the sound mode must only be considered and the scattering of sound by vortical flows can be interpreted like a vorticity–sound modes coupling. The boundary problem can also be analysed in terms of sound and vorticity modes generation at the boundary. In the context of sound scattering by vortical flows, we must consider the influence of the mean flow on the boundary treatment. The compressible vortical flow may produce sound waves from vorticity–sound and sound–sound interactions. It may also generate vorticity waves from vorticity–vorticity interactions at the boundary. Thus, the sound and vorticity generation

properties at the boundary have to be analysed. We must also consider the effects of the acoustic waves which can produce sound waves from sound–sound interactions: the sound reflection properties at the boundary must also be studied.

Thus, the following tests are performed. First, we analyse the robustness of the proposed hierarchy of implementations with respect to the mean flow topology. Second, we consider the mean flow influence on the boundary algorithm efficiency and we analyse the sound and vorticity generation at an open boundary. Third, we focus on the sound–sound interactions at the boundary and we carefully analyse the dependency of the reflection properties upon the incidence angle, the frequency and sound value amplitude.

4.1. Implementation robustness

The robustness of the proposed hierarchy of implementations in front of the mean flow topology is analysed in this section. As shown in Section 3.2, the mean flow field values at the boundary can invalidate the boundary algorithm. We investigate the influence of two single vortices, located at the center of the numerical domain, on the boundary implementations. The first vortical flow, with a zero circulation, is localized far from the boundaries (the fluid is at rest at the boundaries). The second vortical flow has a circulation. In this case, a mean flow occurs at the boundaries and the assumptions (38) may break down. Some computations have been performed with open non-reflecting boundaries and some with a non-reflecting plane emitter over the western boundary. The chosen value for the velocity amplitude $u_0 = 10^{-2}$ m s^{-1} ensures that the sound waves entering the computational domain are linear (see Section 4.3.2.2).

These tests were made with the three implementations and two different mean flows of great importance in scattering problems (see Section 5 and [52]):

- a Taylor vortex [53] (zero circulation flow) whose vorticity is

$$\overrightarrow{\Omega}_1(r) = \omega_1(2 - (r/L_1)^2)\exp\left[\frac{1-(r/L_1)^2}{2}\right]\hat{z} \tag{46}$$

  with L_1 the typical size of the vortex core and ω_1 its maximum vorticity. $\mathscr{M}_1 = |\omega_1|L_1/c$ is the Mach number based on the flow. The velocity field,

$$\overrightarrow{U}_1(r) = \omega_1 r\exp\left[\frac{1-(r/L_1)^2}{2}\right]\hat{\theta}, \tag{47}$$

  where $\hat{\theta}$ is the orthoradial unit vector, is almost zero for $r \geqslant 4L_1$.
- an Oseen vortex [54] whose vorticity is

$$\overrightarrow{\Omega}_2(\vec{r}) = \omega_2\exp\left[-\alpha\frac{r^2}{L_2^2}\right]\hat{z}. \tag{48}$$

  The corresponding velocity field is

$$\overrightarrow{U}_2(\vec{r}) = \frac{\Gamma_2}{2\pi r}\left(1-\exp\left[-\alpha\frac{r^2}{L_2^2}\right]\right)\hat{\theta}, \tag{49}$$

  where $\hat{\theta}$ is the orthoradial unit vector and $\alpha = 1.256431$ a constant such that the flow velocity maximum is located at $r = L_2$. The vortex circulation is $\Gamma_2 = \omega_2\pi L_2^2/\alpha$ and its Mach number is $\mathscr{M}_2 = |\omega_2|L_2/[(1+2\alpha)c]$.

There is a major difference between these two vortical flows: the Taylor vortex is localized ($\overrightarrow{U}_1 = \overrightarrow{0}$ for $r \geqslant 4L_1$) whereas the velocity field of an Oseen vortex extends over the entire space, slowly decaying as $1/r$ far from the vortex core. Conditions (38) can always be satisfied with the Taylor vortical flow if the boundary is located at a distance larger than $4L_1$ from the core, whereas $l_0 \simeq r$ for the Oseen vortex. Moreover, the criterion for the validity of implementation I_3 is easier to satisfy for the Taylor flow than for the Oseen one.

The mean flows characteristics are:

- $\mathscr{M}_1 \simeq 0.16$ and $L_1 = 0.01$ m for the Taylor vortex;
- $\Gamma_2 \simeq 5.0$ m^2 s^{-1}, $\mathscr{M}_2 \simeq 0.15$ and $L_2 = 0.01$ m for the Oseen vortex.

Two different computational domains have been used: domain 1 (size $l_1 \times l_1$, uniform cartesian grid with 256×256 points and a spatial resolution $\Delta = 7.81 \times 10^{-4}$ m) and domain 2 (size $l_2 \times l_2$, uniform cartesian grid with 512×512 points, $\Delta = 7.81 \times 10^{-4}$ m). The same time step $\mathrm{d}t = 10^{-6}$ s is chosen with the two computational domains.

For the three implementations and the two computational domains, the temporal evolution of the mean flow density at the center of the domain (ρ_c^k for domain k) and at the middle of the eastern boundary (ρ_{em}^k for domain k) have been recorded.

Fig. 2 shows the temporal evolution of the flow density ρ_c^k for the Taylor vortex flow and for the three possible implementations. Except from small differences due to the domain size, the three implementations give the same result. The temporal evolution of the density ρ_c^k (resp. ρ_{em}^k) for the Oseen vortex flow is plotted on Fig. 3 (resp. Fig. 4) for the three proposed implementations. At both recording locations, the results are similar: implementations I_1 and I_2 ensure numerical stability, whereas a numerical instability occurs for implementation I_3. Its growth rate depends on the computational domain size. This instability is related to the presence of a mean flow which violates condition (38) for implementation I_3. Fig. 5 (bottom) shows the temporal evolution of the density ρ_c^k for the Oseen vortex flow when a sound wave propagates through the mean flow. The presence of a sound wave interacting with the mean flow does not change the starting time of this numerical instability.

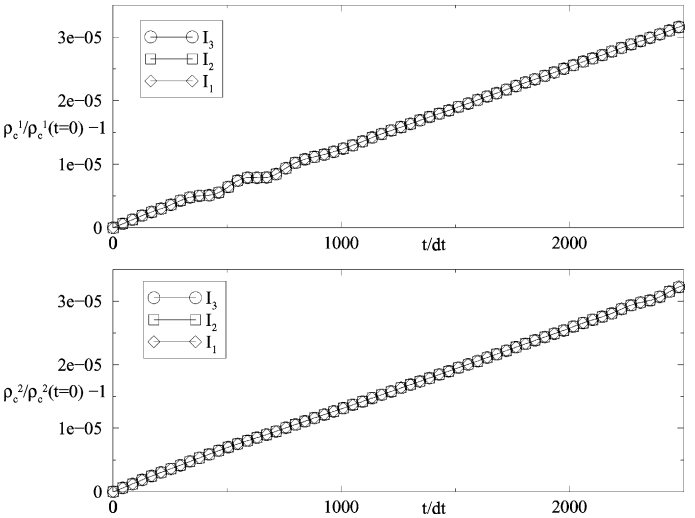

Fig. 2. Taylor vortex alone: $\rho_c^1/\rho_c^1(t=0) - 1$ (top) and $\rho_c^2/\rho_c^2(t=0) - 1$ (bottom) at the center of the computational domain versus $t/\mathrm{d}t$. (◇) implementation I_1; (□) implementation I_2; (○) implementation I_3.

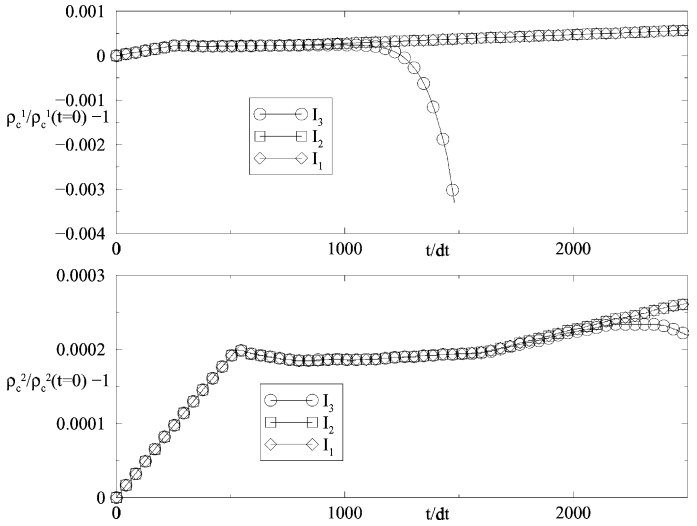

Fig. 3. Oseen vortex alone: $\rho_c^1/\rho_c^1(t=0)-1$ (top) and $\rho_c^2/\rho_c^2(t=0)-1$ (bottom) at the center of the computational domain versus $t/\mathrm{d}t$. ($\diamondsuit$) implementation I_1; ($\square$) implementation I_2; ($\bigcirc$) implementation I_3.

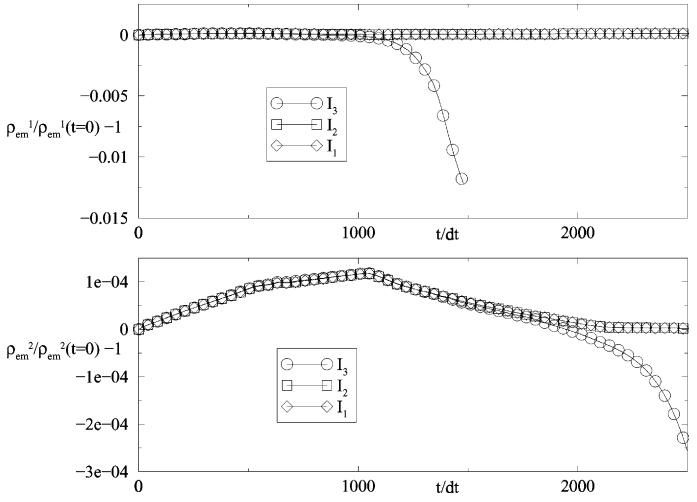

Fig. 4. Oseen vortex alone: $\rho_{em}^1/\rho_{em}^1(t=0)-1$ (top) and $\rho_{em}^2/\rho_{em}^2(t=0)-1$ (bottom) at the middle of the East boundary. ($\diamondsuit$) implementation I_1; ($\square$) implementation I_2; ($\bigcirc$) implementation I_3.

4.2. Acoustic and vorticity generations from the mean flow-boundaries interactions

In this section, the influence of the mean flow vorticity on the boundary algorithm property is analysed. As pointed out before, the interaction of the mean flow vorticity mode with the boundary may generates sound and vorticity waves which propagate within the computational domain. We also want to analyse the efficiency of the boundary algorithm when the underlying approximations (Section 3.2) break down. It is clear from the above tests that implementations I_1 and I_2 should only be analysed here.

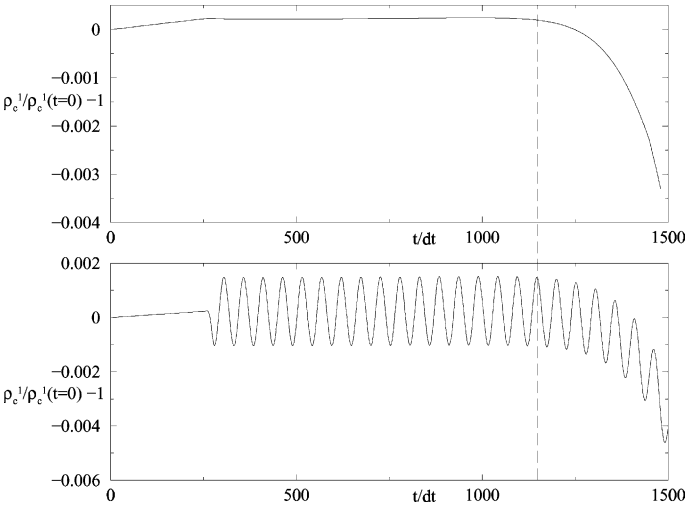

Fig. 5. Oseen vortex alone: $\rho_c^1/\rho_c^1(t=0)-1$ at the center of the computational domain versus $t/\mathrm{d}t$ for implementation I_3. Top: mean flow alone. Bottom: sound and mean flow. The dashed line indicates the beginning of the numerical instability.

We consider a square computational domain (size $l_1 \times l_1$, uniform cartesian grid with 192×192 points, spatial resolution $\Delta = 7.81 \times 10^{-4}$ m). A zero circulation Taylor vortex (46) is advected by a uniform flow U_0 and crosses the eastern boundary. Non-reflecting boundary conditions are imposed at the north, south and east boundaries and an isothermal inlet with constant velocity U_0 at the west boundary. The velocity field is:

$$\begin{pmatrix} u \\ v \end{pmatrix} = \begin{pmatrix} U_0 \\ 0 \end{pmatrix} + \overrightarrow{U}_1. \tag{50}$$

We choose $L_1 = 0.01$ m and $U_0/c = 0.26$ to get a subsonic outflow. The vortex core reaches the eastern boundary at $t/\mathrm{d}t = 750$. Two tests are performed with different Mach numbers $\mathscr{M}_1$ based on the vortical flow (47): $\mathscr{M}_1 \simeq 0.16$ and $\mathscr{M}_1 \simeq 0.48$.

In each case, the temporal evolution of the absolute value of the total vorticity $\omega_{\mathrm{abs}} = \int |\omega| \mathrm{d}^2 r$ (Fig. 6) and of the maximum vorticity $\omega_{\max}$ (Fig. 7) have been computed. For the smallest Mach number ($\mathscr{M}_1 \simeq 0.16$), both implementations lead to the same result: the total vorticity and the maximum vorticity decrease in the same way when the vortex crosses the boundary. For the largest Mach number ($\mathscr{M}_1 \simeq 0.48$), implementation I_2 leads to an instability, whereas the vortex crossing can be computed with implementation I_1. This result has to be related to the approximations required for the algorithms validity (see Eq. (38)). These conditions are not satisfied for the linear implementation I_2. The conditions are weaker for implementation I_1 as the characteristic waves are computed from the full physical values at the boundary. It should be noted that for the same reasons, the residual vorticity is one order of magnitude larger using implementation I_2 than using implementation I_1 for $\mathscr{M}_1 \simeq 0.16$ (see Fig. 7). Figs. 8 and 9 show the vorticity field and the density field, computed using implementation I_1, when the vortex crosses the boundary, for $\mathscr{M}_1 \simeq 0.16$ and $\mathscr{M}_1 \simeq 0.48$, respectively. In both cases, the vortex is distorted when it reaches the outlet because the boundary treatment is 1D. As the flow is isentropic, only acoustic waves and vorticity waves are generated at the boundary [1]. They propagate upstream and induce inlet perturbations which can produce numerical instabilities. This boundary coupling effect is analysed in details by Poinsot and Lele [27]. It should be noted that this instability only slightly depends on the western boundary choice: the boundary treatment applies only on the fluctuating part of flow $\widehat{V}$. Thus, setting an inlet condition or a non-reflective

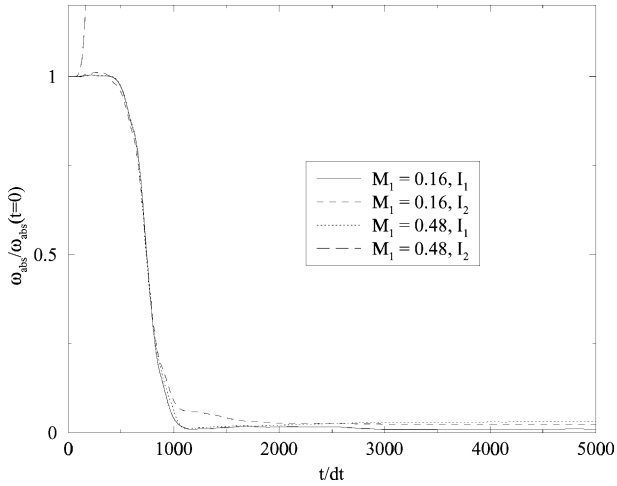

Fig. 6. Time evolution of the total absolute vorticity ω_{abs} normalized by its initial value for implementations I_1 and I_2.

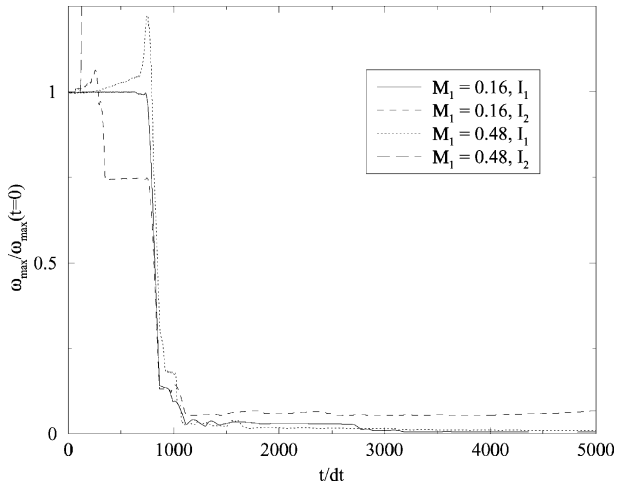

Fig. 7. Time evolution of the maximum vorticity ω_{max} normalized by its initial value for implementations I_1 and I_2.

condition at the western boundary does not prevent this numerical instability. It is clear that the larger the vortex strength is, the stronger the numerical instabilities are but the residual vorticity remains less than 1% of the initial vorticity in our computations. The outflow implementation I_1 thus allows to compute large Mach number vortices and is rather satisfactory for the mean flow field (vortex). Nevertheless, it remains unsatisfactory for the acoustic part (Figs. 8 (bottom) and 9 (bottom)). Improvements of the boundary outlet can be made, with an exit zone (or buffer zone) and some filtering procedures. These enhancements are analysed in many recent papers [29,48,50] and can significantly improve the boundary treatment for such physical problems. We do not discuss this point here: this test is only performed to analyse the efficiency of the boundary algorithms I_1 and I_2 and the perturbations generation at the boundary. Please keep in mind that in most of the scattering analyses, the mean flow vorticity vanishes at the boundaries (the sound wave analysis is often performed in the far-field approximation).

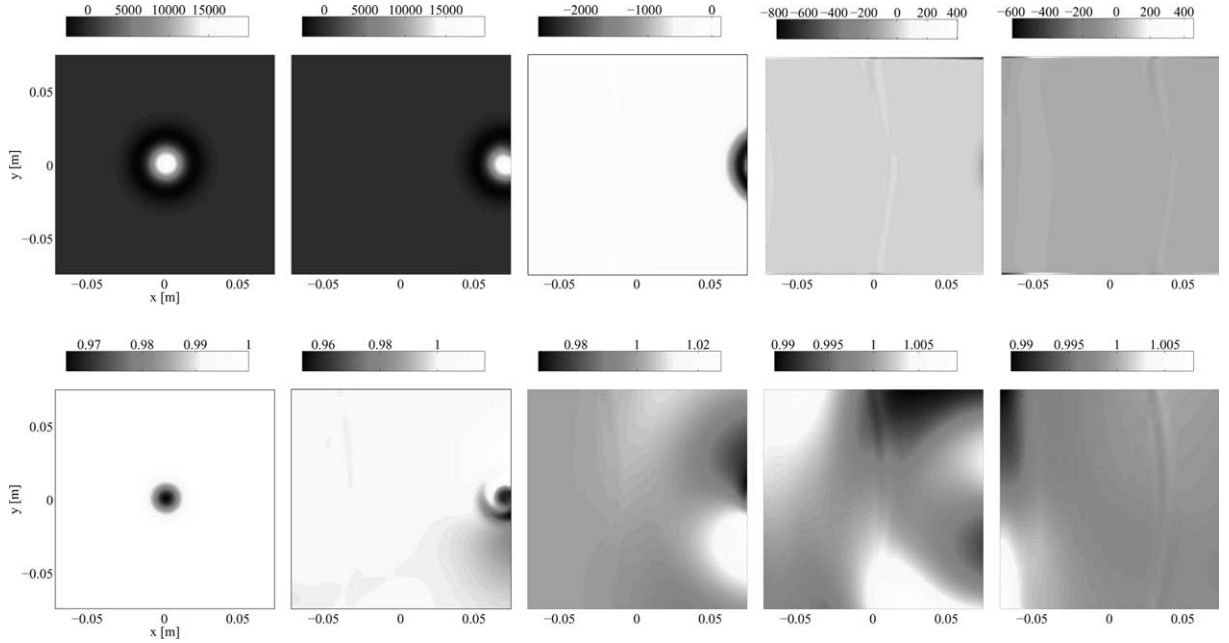

Fig. 8. Vorticity field (top) and density field (bottom) of a Taylor vortex (46) (vortex mach number $\mathscr{M} \simeq 0.16$) propagating through the eastern boundary, for implementation I_1. From left to right: $t/\mathrm{d}t = 0$, $t/\mathrm{d}t = 800$, $t/\mathrm{d}t = 1000$, $t/\mathrm{d}t = 1200$ and $t/\mathrm{d}t = 1500$.

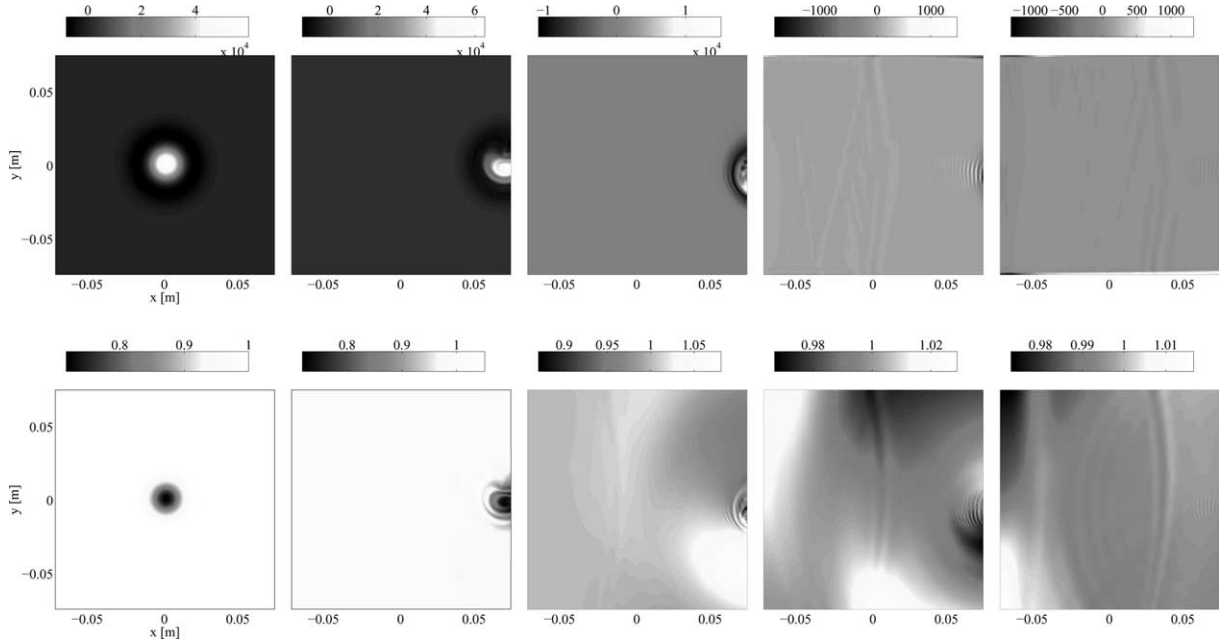

Fig. 9. Vorticity field (top) and density field (bottom) of a Taylor vortex (46) (vortex mach number $\mathscr{M} \simeq 0.48$) propagating through the east boundary, for implementation I_1. From left to right: $t/\mathrm{d}t = 0$, $t/\mathrm{d}t = 800$, $t/\mathrm{d}t = 1000$, $t/\mathrm{d}t = 1200$ and $t/\mathrm{d}t = 1500$.

4.3. Evaluation of the sound reflection properties

This section is devoted to the evaluation of sound wave reflections properties of the boundary algorithm. A frequency range corresponding to ultrasounds (wavelength close to the vortex size) and a small amplitude (linear waves, see paragraph Section 4.3.2.2) have been used in agreement with typical values used in experimental studies of sound scattering [5,6,8,9,13]. In an isentropic flow, the pressure can be easily related to the density with Eq. (8). Thus, we only consider in the following the fluid density ρ.

Three different tests have been performed:

1. sound radiation by a single point source located at the center of the computational domain, with open non-reflecting boundaries;
2. sound radiation by a single non-reflecting sound emitter located at the western side of the computational domain, with open non-reflecting boundary conditions at the three other boundaries. The reflection analysis has been performed with respect to the sound wave frequency and amplitude;
3. sound radiation by both a non-reflecting linear sound emitter located at the western side and a linear sound emitter located at the center of the computational domain, with open non-reflecting boundary conditions at the three other boundaries.

Each of these basic tests is relevant to a particular aspect of the numerical simulation of scattering problems as the sound field may be decomposed into a plane wave and a locally cylindrical wave (see Eqs. (2) and (3)). When the perturbations are small and the fluid at rest, the three boundary conditions implementations are similar. Thus, all the results presented in this section are based on implementation I_3. For each test, one of the two configurations I or II (Fig. 10) is used and two numerical computations are made: one with the computational domain 1 of size $l \times l$ (numerical result V_1) and a second one with the computational domain 2 of size $2l \times 2l$ (numerical result V_2). The reflection properties of the algorithm are estimated using the reflected density at a given point M of the domain 1 boundary

$$\rho_r(M) = \rho_1(M) - \rho_2(M). \tag{51}$$

The reflected wave is analysed at the middle point (B) and a corner point (A) of a boundary of domain 1 (Fig. 10). At point B, one can expected the best results from the boundary condition procedure as the sound waves propagation direction is normal to the boundary, an underlying assumption of the 1D characteristic boundary approach. At point A, we likely obtain the worst result which allows to give an upper bound for the reflected wave amplitude.

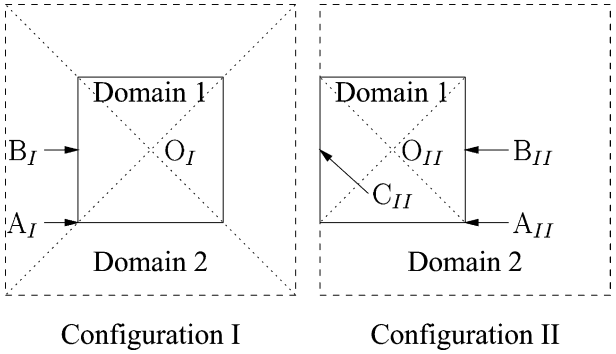

Fig. 10. Configuration I used for test 1 (left) and configuration II used for tests 2 and 3 (right). Reflections are analysed at points A_I and B_I or at points A_{II}, B_{II} and C_{II}.

4.3.1. Point source

A point sound emitter is located at point O_I of the numerical configuration I (Fig. 10) with

$$\rho_s(O_I) = \rho_{0s} \sin(2\pi\nu t). \tag{52}$$

For this test, $l = 0.2$ m and $\rho_{0s} = 2 \times 10^{-4}$ kg m^{-3} to ensure that the outgoing cylindrical waves are linear. A space step $\Delta = 7.81 \times 10^{-4}$ m (corresponding to a uniform grid of 256×256 points in domain 1) and a time step $dt = 10^{-6}$ s are chosen and each boundary is an open non-reflecting boundary. Computations are performed for different sound wavelengths $\lambda = c/\nu$ and the reflected waves are analysed at points A_I and B_I. Computations are stopped before the reflected waves from the north-west and south-west corners reach point B_I, in order to make an accurate analysis at the western boundary. Fig. 11 shows the sound wave density and the reflected sound wave at point B_I. As one can expect, after a transient time, the reflected wave amplitude is small (about 0.6% of the incident wave magnitude). Fig. 12 shows the density of the incident reflected waves at point A_I. The situation is very different from the one at point B_I because the cylindrical sound wave is no longer perpendicular to any of the boundaries. Thus, the reflected wave amplitude is larger and may reach values as high as 38% of the incident wave magnitude. This case is the worst situation one may encounter in scattering simulations. We have also performed the same analysis at the center of the boundary domain $[A_I, B_I]$ (results not presented). In this case, the reflected wave amplitude is around 6% of the incident wave magnitude. It should be note that these results do not seem to depend on the incident wavelength λ for large wavelengths, where the scheme dispersion and damping effects are negligible (see Appendix A).

4.3.2. Non-reflecting plane emitter alone

A wave emitter is located at the western boundary in the configuration II (including point C_{II}, see Fig. 10). $l = 0.1$ m, $\Delta = 7.81 \times 10^{-4}$ m and $dt = 10^{-6}$ s. A uniform mesh with 128×128 grid points is used in domain 1 and the three remaining boundaries are open non-reflecting boundaries. We analyse two properties of the open non-reflecting boundary: frequency range and amplitude range of validity.

4.3.2.1. Pulse forcing. An acoustic Gaussian pulse is emitted at the western boundary. The sound wave velocity at the boundary is, from Eq. (42),

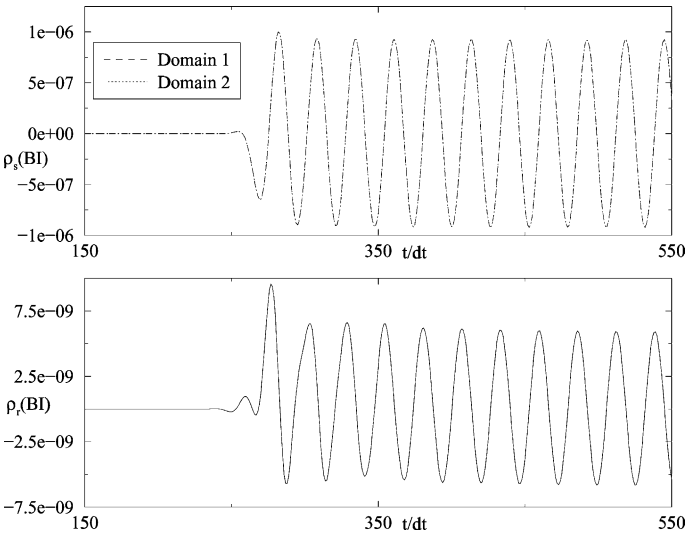

Fig. 11. Top: sound wave density $\rho_s(B_I)$ (kg m^{-3}) in domains 1 and 2 versus t/dt, for $\lambda = 0.01$ m. Bottom: the corresponding reflected wave $\rho_r(B_I)$ (kg m^{-3}) versus t/dt.

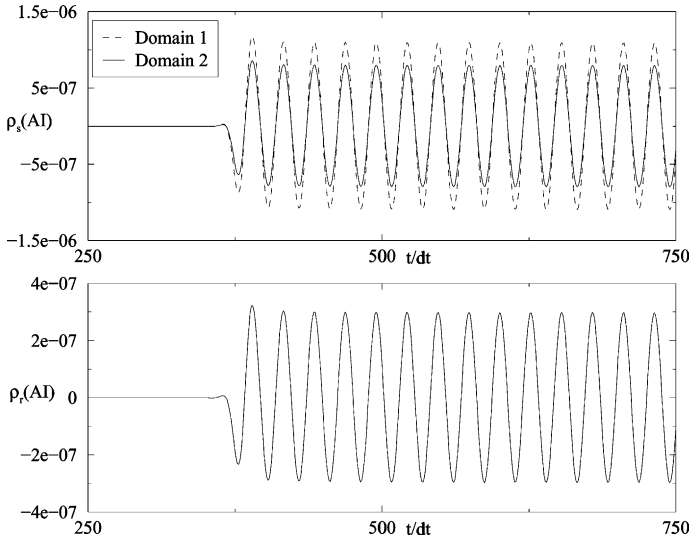

Fig. 12. Top: sound wave density $\rho_s(A_I)$ (kg m^{-3}) in domains 1 and 2 versus t/dt, for $\lambda = 0.01$ m. Bottom: the corresponding reflected wave $\rho_r(A_I)$ (kg m^{-3}) versus t/dt.

$$u_s = u_{0s}\sin(2\pi v_0 t)\exp\left[-\left(\frac{t-to}{\tau}\right)^2\right]. \tag{53}$$

The Gaussian envelope width is $\tau = 2.5 \times 10^{-5}$ s and the emitter amplitude maximum occurs at $t_0 = 1.5 \times 10^{-4}$ s. This test allows to test the frequency behavior of our boundary treatment. Computations are made with two different central frequencies v_0 and the sound waves are analysed at point B_{II} of the two domains 1 and 2. Figs. 13 and 14 show the density for the two acoustic pulses $v_0 = 50$ kHz

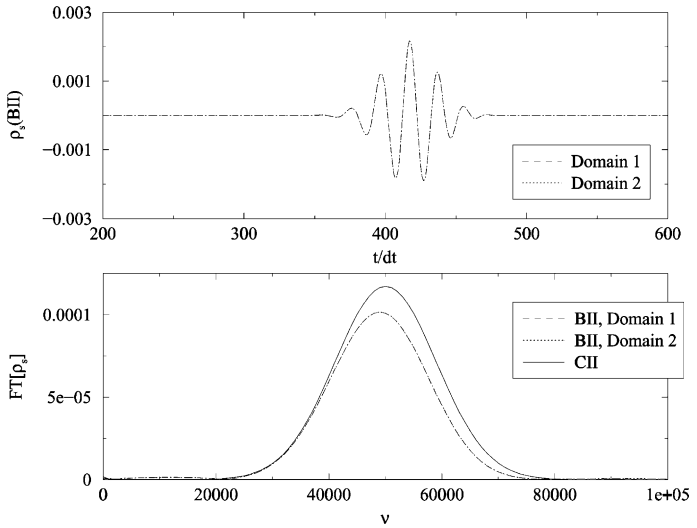

Fig. 13. Top: acoustic pulse density $\rho_s(B_{II})$ (kg m^{-3}) in domains 1 and 2 versus t/dt. The central pulse frequency is $v_0 \simeq 50$ kHz. Bottom: the corresponding Fourier spectra and the Fourier spectrum of the emitted acoustic pulse, computed at the point C_{II}.

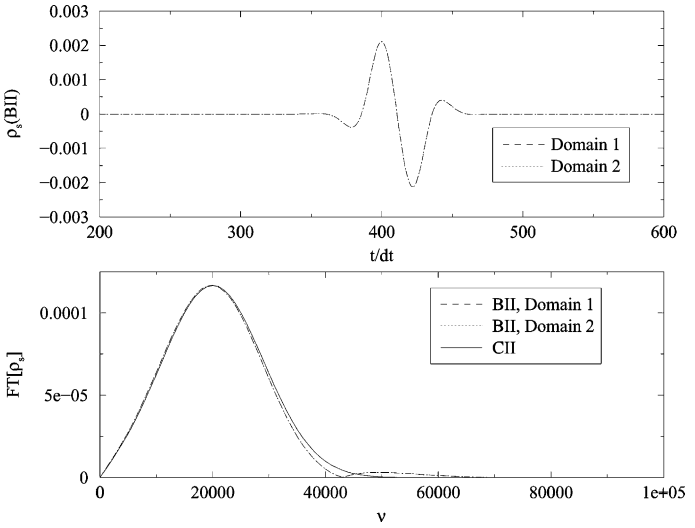

Fig. 14. Top: acoustic pulse density $\rho_s(B_{II})$ ($kg\,m^{-3}$) in domains 1 and 2 versus t/dt. The central pulse frequency is $v_0 \simeq 15$ kHz. Bottom: the corresponding Fourier spectra and the Fourier spectrum of the emitted acoustic pulse, computed at point C_{II}.

($\lambda_0 = 7.6 \times 10^{-3}$ m) and $v_0 = 20$ kHz ($\lambda_0 = 1.9 \times 10^{-2}$ m) at point B_{II} and their temporal Fourier spectra. We have also plotted, on the same part of the figure, the Fourier spectrum of the initial acoustic pulse, computed at the point C_{II} of the emitter. The high frequencies of the acoustic pulse are damped when the pulse propagates through the computational domain (see Figs. 13 (bottom) and 14 (bottom)). This numerical damping comes mainly from the interior scheme: wavelengths smaller than 10 grid size cannot accurately propagate because numerical dispersion and damping become important (see Appendix A and [52]). This limit corresponds to a cutoff frequency $v_c \simeq 48$ kHz, in agreement with the spectral analysis. Figs. 15 and 16 show the reflected waves at point B_{II} and their Fourier spectra for $v_0 = 50$ kHz and $v_0 = 20$ kHz, respectively. The reflected wave is weaker for the lowest frequency. Both spectra exhibit the same shape with a maximum around the central frequency of the pulse. In addition, the spectra have a high frequency part which do not correspond to any frequency in the incident pulse. These high frequencies may be related to spurious numerical reflections at the boundary due to inaccuracies in the numerical dispersion relation [55], which generate sound waves with a few grid points wavelength (e.g., 100 kHz corresponds to a five grid points wavelength). Let us define, at a given point M of the domain 1 boundary, the reflection coefficient $\mathscr{R}_{FT}(M, v)$ in the Fourier space

$$\mathscr{R}_{FT}(M, v) = \frac{FT(\rho_r(M, t))}{FT(\rho_{s2}(M, t))}. \tag{54}$$

The Fourier spectrum around the central pulse frequency v_0 is analysed and $\mathscr{R}_{FT}(B_{II}, v)$ is computed in the frequency range $[v_0/\sqrt{2}, v_0 + (v_0 - v_0/\sqrt{2})]$. Fig. 17 shows the log–log plot of $\mathscr{R}_{FT}(B_{II}, v)$ with the frequency v. $\mathscr{R}_{FT}(B_{II}, v)$ increases with the frequency. However, $\mathscr{R}_{FT}(B_{II})$ remains less than 1% in the frequency range, where the numerical simulations can be performed with low numerical dispersion and low numerical damping.

We conclude this section by analysing the propagation of a monochromatic linear wave through the eastern open boundary. The sound wave velocity at the boundary is, from Eq. (42),

$$u_s = u_{0s} \sin(2\pi v t). \tag{55}$$

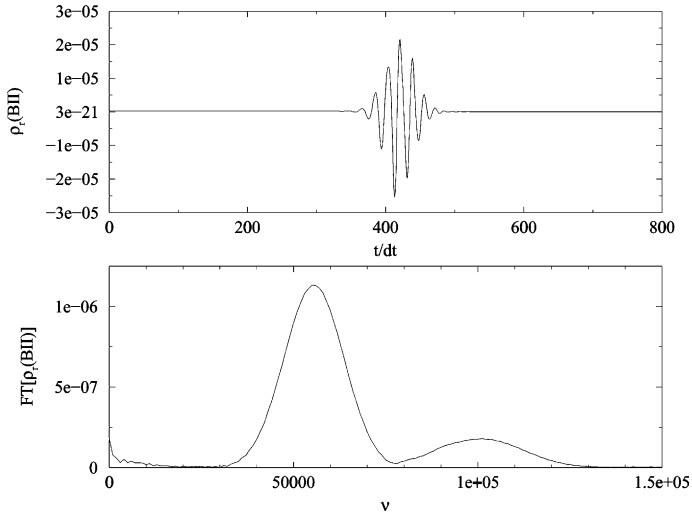

Fig. 15. Top: reflected sound wave density $\rho_r(B_{II})$ (kg m^{-3}) versus t/dt. The central frequency of the initial pulse is $v_0 \simeq 50$ kHz. Bottom: the corresponding Fourier spectrum.

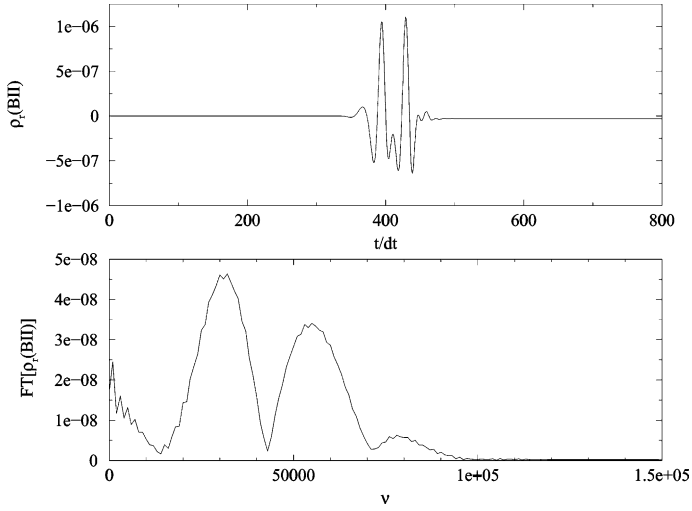

Fig. 16. Top: reflected sound wave density $\rho_r(B_{II})$ (kg m^{-3}) versus t/dt. The central frequency of the initial pulse is $v_0 \simeq 15$ kHz. Bottom: the corresponding Fourier spectrum.

The plane emitter is monochromatic and the emitted acoustic waves are linear: $u_{0s} = 10^{-2}$ m s^{-1} to ensure this property (see paragraph Section 4.3.2.2). Computations have been made for different wavelengths $\lambda = c/v$ and the reflected wave is computed at points A_{II} and B_{II}. As the incident plane wave reaches the boundary with a normal incidence, the reflected wave is the same at points A_{II} and B_{II}.

Fig. 18 shows the reflected wave for $\lambda = 0.02$ m (top) and $\lambda = 0.01$ m (bottom). After a transient time due to the sound wave arrival at the boundary (a reflected wave with a few Δ wavelength is generated, see Fig. 18 (top), where this small effect is visible because the reflected wave has a small amplitude), the reflected amplitude is five times smaller for $\lambda = 0.02$ m (26 grid points per wavelength) than for $\lambda = 0.01$ m (13 grid

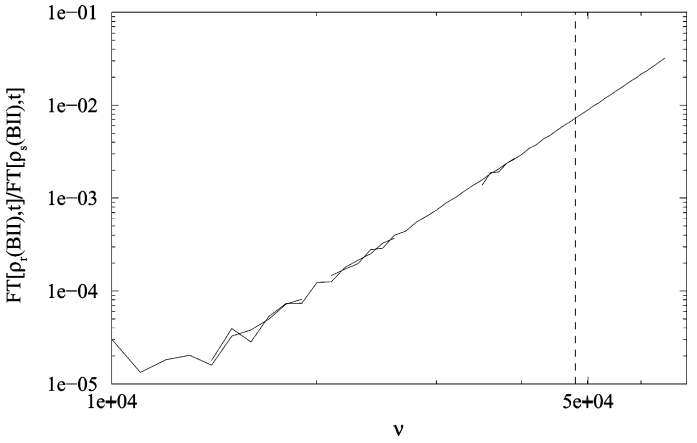

Fig. 17. Log–log plot of the reflection coefficient $\mathscr{R}_{FT}(B_{II}, \nu)$ versus the frequency ν. The dashed line roughly shows the cut-off frequency of the interior scheme (see Fig. 32).

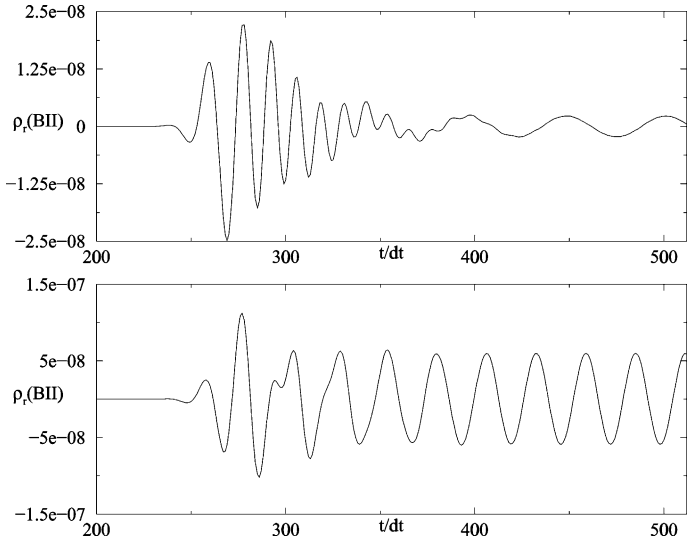

Fig. 18. Reflected wave $\rho_r(B_{II})$ (kg m^{-3}) versus t/dt. Top: $\lambda = 0.02$ m. Bottom: $\lambda = 0.01$ m.

points per wavelength). As expected, the larger the number of mesh points per wavelength is, the smaller the amplitude of the reflected waves is.

4.3.2.2. Influence of the forcing amplitude. In this paragraph, the plane emitter is monochromatic (Eq. (55) with $\nu \simeq 19$ kHz) but the acoustic waves amplitude u_{0s} is varied up to the non-linear regime. In a fluid at rest, linear acoustic remains valid as long as $\rho_s \ll \rho_{ref}$ i.e. $u_s \ll c$, where c is the speed of sound [56]. Thus, non-linear waves are expected when u_{0s} increases. Fig. 19 shows the time evolution of the sound density at point B_{II} for $u_{0s}/c = 2.63 \times 10^{-5}$ and $u_{0s}/c = 1.32 \times 10^{-2}$. Non-linearities in the sound propagation are observed for $u_{0s}/c = 1.32 \times 10^{-2}$. Choosing $u_{0s} = 10^{-2}$ m s^{-1} ($u_{0s}/c = 2.63 \times 10^{-5}$) leads to linear acoustic waves, as mentioned above. The reflected sound wave density at point B_{II} is displayed on Fig. 20, for $u_{0s}/c = 2.63 \times 10^{-5}$ (top) and $u_{0s}/c = 1.32 \times 10^{-2}$ (bottom). It shows the dependency of the reflection

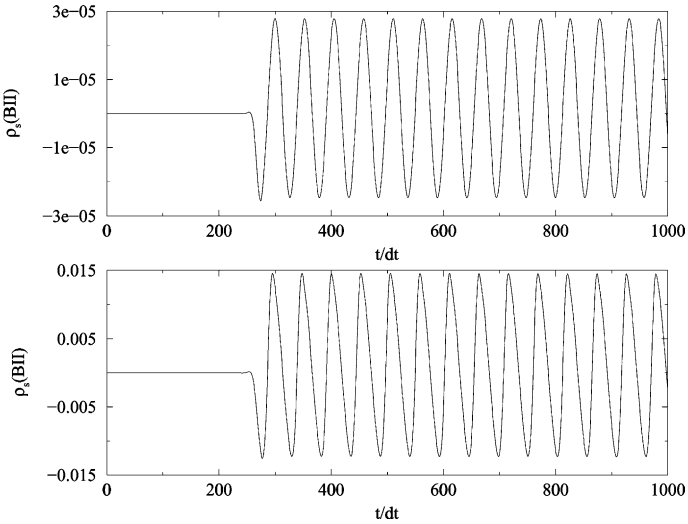

Fig. 19. Sound wave density $\rho_s(B_{II})$ (kg m^{-3}) in domain 2 versus t/dt, for $u_{0s}/c = 2.63 \times 10^{-5}$ (top) and $u_{0s}/c = 1.32 \times 10^{-2}$ (bottom).

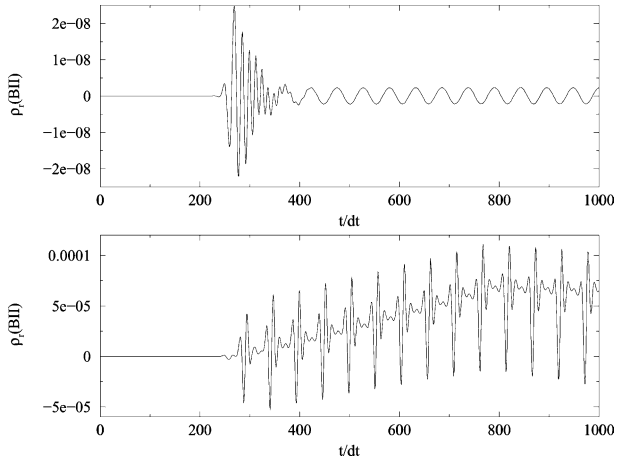

Fig. 20. Reflected sound wave density $\rho_r(B_{II})$ (kg m^{-3}) versus t/dt. Top: $u_{0s}/c = 2.63 \times 10^{-5}$. Bottom: $u_{0s}/c = 1.32 \times 10^{-2}$.

properties on the incident amplitude. To estimate this effect, the reflective coefficient $\mathscr{R}(\mathscr{M})$ at a given point M of the domain 1 boundary is computed after the transient time when the sound wave arrival at the boundary (see Fig. 20 (top))

$$\mathscr{R}(M) = \frac{\rho_{0_r}(M)}{\rho_{0_{s2}}(M)} \tag{56}$$

under the same notations that in Eq. (52). For non-linear waves, ρ_{0_r} and $\rho_{0_{s2}}$ cannot be computed from their rms values. Thus, half of the difference between the maximum and minimum density values are used instead. The $\mathscr{R}(M)$ estimations are presented in Table 1. These values proved to be independent of the chosen implementation I_1, I_2 or I_3, even for large incident amplitude. As pointed out in [51], the reflection strongly

Table 1
Evolution of $\mathscr{R}(\mathscr{B}_{II})$ with the sound wave amplitude

u_{0s}/c	2.63×10^{-6}	2.63×10^{-5}	2.63×10^{-4}	2.63×10^{-3}	1.32×10^{-2}	2.63×10^{-2}
$\mathscr{R}(\mathscr{B}_{II})$	8.56×10^{-5}	8.61×10^{-5}	8.81×10^{-5}	2.27×10^{-4}	4.11×10^{-3}	2.75×10^{-2}

increases for increasing wave amplitude but remains small, even for amplitudes such that non-linearities play a significant role during the sound propagation.

4.3.3. Non-reflecting plane emitter and pulse emitter

The last test is performed using the same configuration and the same parameters as in the previous section. An additional linear vertical emitter is located in the middle of domain 1 (including point O_{II}), in configuration II (see Fig. 10). The sound velocity of this emitter is:

$$u_s = u_{1s} \sin(2\pi\nu t). \tag{57}$$

The sound emission is limited to a wave train of 2.5 periods for $\lambda = 0.01$ m ($1/\nu = 2.63 \times 10^{-5}$ s) and $u_{1s} = 8u_{0s}$. Fig. 21 (top) shows the temporal evolution of the density at point C_{II}, when both emitters are activated ($\rho_s(C_{IIb})$) and when the western side emitter is alone ($\rho_s(C_{IIa})$ from the second test). Except when the pulse crosses the boundary, both signals are the same. To validate this result, the sound wave density generated by the pulse emitter is computed at points B_{II} and C_{II}

$$\rho_p(C_{II}) = \rho_s(C_{IIb}) - \rho_s(C_{IIa}). \tag{58}$$

A comparison between $\rho_p(C_{II})$ and $\rho_p(B_{II})$ is presented on Fig. 21 (bottom). As point O_{II} is not exactly at the center of domain 1, a small phase shift between the two signals is observed. Apart from this shift, the signals at the open non-reflecting boundary (point B_{II}) and at the non-reflecting plane emitter boundary (point C_{II}) are identical. Thus, the western boundary behaves like the eastern one for outgoing waves and can be considered as a non-reflecting plane emitter with the same reflected properties as the eastern boundary.

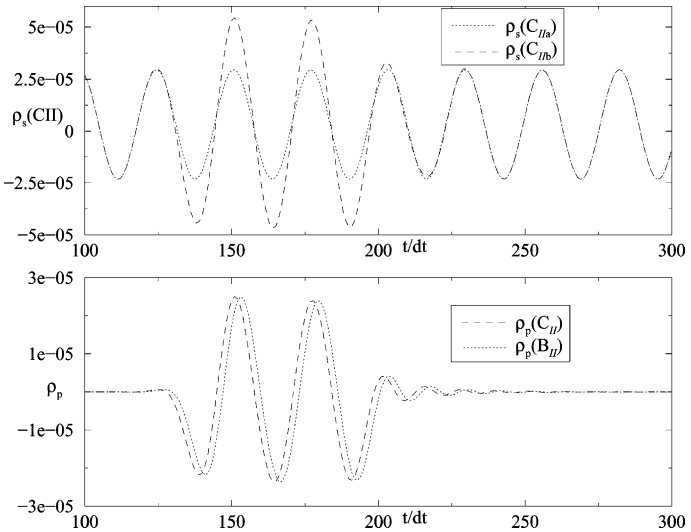

Fig. 21. Top: sound wave density $\rho_s(C_{IIb})$ and $\rho_s(C_{IIa})$ (kg m^{-3}) versus $t/\mathrm{d}t$. Bottom: sound pulse density $\rho_p(C_{II})$ and $\rho_p(B_{II})$ (kg m^{-3}) versus $t/\mathrm{d}t$.

4.4. Summary

The above results shows that the most efficient procedure for a good boundary treatment is implementation I_1. It is the most general decomposition of the physical fields at a boundary and it requires more flexible numerical conditions than implementation I_2 proposed in [29], because it keeps physical informations about the reference mean flow V_0 and the fluctuating part $\widehat{V}$ at the boundary (Eqs. (27) and (29)). Thus, implementation I_1 allows the numerical computation of a wide range of physical situations. Moreover, the acoustical reflections at the boundary always remain small, except when the acoustic wave reaches the boundary in a direction far from the normal incidence, a well-known problem in characteristics methods [43]. In addition, scattering problem in non-linear acoustic can be consider using implementation I_1.

Procedure I_3 is the easiest to implement in a numerical code. However, its validity may be strongly limited by the topology of the mean flow and has to be checked. For many scattering studies, validity conditions for implementation I_3 are satisfied at the boundaries so that I_3 remains a good procedure for a numerical boundary algorithm. This is mostly a consequence of the far-field approximation which must be satisfied to compute the scattering amplitude $f(\theta)$ (Eq. (3)). Thus, most of the scattering results of the next section have been computed with implementation I_3. When implementation I_1 is used, we will explicitly mention it.

5. Sound scattering tests

In order to validate the numerical algorithm for scattering problems, computations of sound scattering problems are performed. To satisfy the far-field approximation, a computational domain of size $l \times l$ with $l \gg L$ is chosen. The scattering amplitudes $f(\theta)$ are computed for both the scattering of a plane sound wave by a Taylor vortex and a vortex dipole, and compared with theoretical results on scattering [10]. The former is a simple zero-circulation flow (mean flow at rest at the boundary). Thus, an analysis of the parasitic sound waves in the study of scattering processes can be performed. Previous tests showed that spurious reflections cannot be entirely avoided using the proposed boundary procedure, especially when waves reach the boundary in a direction far from the normal incidence. An order of magnitude analysis shows however that this algorithm is accurate enough for sound scattering problems. The latter, a more complicated flow structure, allows us to test the validity of our boundary algorithm for a weakly unsteady flow. A last test, where a sound wave experiences multiple scattering by three Oseen vortices for Mach number close to 0.8 is performed. Although no theory is available for comparison purposes, this test shows some complex problem that can be dealt with.

5.1. Sound scattering computations

Two quantities are of central importance in sound scattering studies [57]: the scattered wave density ρ_{scat} and the scattered amplitude $f(\theta)$ (see Eqs. (2) and (3)). ρ_{scat} characterizes the local structure of the sound wave resulting from the scattering process, whereas $f(\theta)$ is related to the scattered acoustic energy and the scattered cross-section, an important quantity to analyse the scattering efficiency.

For a given set of parameters (λ/L for example) and a numerical steady-state flow $U_0 = (\rho_0, \rho_0 u_0, \rho_0 v_0, E_0)^t$, ρ_{scat} and $f(\theta)$ are computed using relations (2) and (3) and the following procedure (see also Fig. 22):

(a) the temporal evolution of the solution $U_{\text{int}}(t)$ resulting from the interaction of the mean flow and the incident sound wave is computed from the initial condition U_0;
(b) the temporal evolution of the mean flow alone $U_f(t)$ is computed from the initial state U_0 without any incident sound wave (in order to take into account any possible distortion of this mean flow by the numerical scheme inaccuracies);

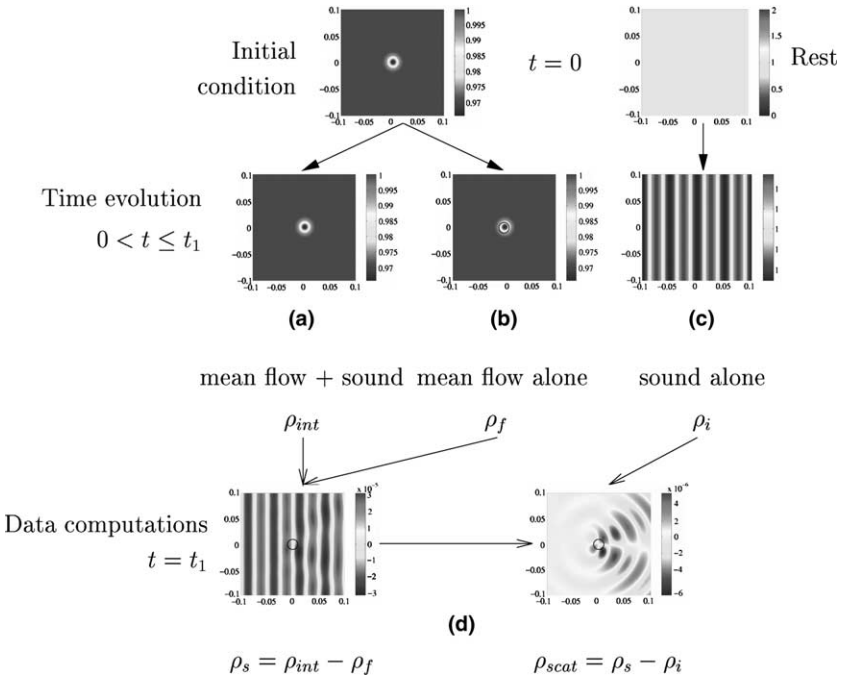

Fig. 22. Computational procedure of the sound quantities.

(c) the temporal evolution of the sound field $U_i(t)$ resulting from the incident sound propagation is computed in the medium at rest (without the mean flow), in order to take into account any possible numerical damping and dispersive effects on the sound waves propagation (see Appendix A);
(d) computation of the total and scattered sound densities:

$$\begin{aligned} \rho_{\mathrm{s}}(\vec{r},t) &= \rho_{\mathrm{int}}(\vec{r},t) - \rho_f(\vec{r},t), \\ \rho_{\mathrm{scat}}(\vec{r},t) &= \rho_{\mathrm{s}}(\vec{r},t) - \rho_i(\vec{r},t), \end{aligned} \tag{59}$$

(e) computation of the scattered amplitude (3) for a set of points located at a given distance $r \gg 2\pi L^2/\lambda$ from the scattering region

$$f(\theta) = \sqrt{r}\rho_{0\mathrm{scat}}/\rho_{0i}, \tag{60}$$

where the subscript 0 denotes the sound wave amplitude.

Using the numerical results from steps (b) and (c) instead of analytical values enables to avoid all the undesirable numerical errors that might result from step (a). A preliminary computation is also performed to get a numerical steady-state flow U_0 from a given analytical steady-state flow U_{a}. U_0 is close but not equal to U_{a}, due to the numerical spatial and temporal discretization errors. Thus, the variables related to the physical scattering processes of the sound wave by the mean flow are only computed at steps (d) and (e), assuming that no perturbation is introduced by the boundary condition algorithm.

5.2. Sound scattering by a Taylor vortex

We consider an axisymmetric zero circulation vortex (Taylor vortex) of typical size L_1, with vorticity given by Eq. (46). $L_1 = 0.01$ m and $\rho_{0i} = 2.63 \times 10^{-5}$ kg m^{-3} ($u_{0i} = 10^{-2}$ m s^{-1}). A uniform mesh with

1024×1024 grid points is used with $l = 0.8$ m to satisfy the far-field approximation. This vortical flow has a zero circulation. Thus, it is possible to analyse the scattering process and its dependencies in $\mathscr{M}_1$ and λ/L_1: one can investigate the sound scattering within and beyond the first Born approximation (see below) [52,58].

5.2.1. Theoretical analysis

The theoretical results on sound scattering have been mostly established for a mean vortical flow interacting with a monochromatic plane wave. The mean flow time scale evolution is assumed to be larger than the sound period (frozen mean flow hypothesis) and only small Mach numbers $\mathscr{M} \ll 1$ are considered. Then, using both the first Born approximation ($2\pi\mathscr{M}L_1/\lambda \ll 1$ [52,58]) and the far-field approximation, the scattering amplitude only depends on the scattering angle θ and on the component of the Fourier transform of the vorticity orthogonal to the scattering plane [10,11]. The scattering amplitude proved to be linear in Mach number and to depend on λ/L via the Fourier transform of the vorticity. As λ/L decreases, the maximum value of the scattering amplitude increases. At the same time, the angular sector, where the forward scattered waves have a significant amplitude is reduced as well as the backscatter phenomenon (see the theoretical results presented on Fig. 23 and please remember that $f \propto \mathscr{M}$).

5.2.2. Comparison with theoretical predictions

Fig. 23 (top) shows both the numerical and the theoretical scattering amplitude in the case $\lambda/L_1 = 10$ and $\mathscr{M}_1 = 0.16$, where the Born approximation is valid. A good agreement is found, even with such a small scattering amplitude (see Fig. 26 and [52,58]). A good agreement is also found for $\lambda/L_1 = 1$ and $\mathscr{M}_1 = 0.016$ (Fig. 23, bottom), a choice of parameter for which the Born approximation is still valid. The small discrepancies can be related to both reflection phenomenons at the boundaries and interior scheme inaccuracies. In order to distinguish between these two sources of inaccuracies, we propose an order of magnitude of the reflections at the boundaries, using the theoretical results presented on Fig. 23. Suppose an incident sound wave of amplitude $A_0 = 1$. First, the reflected waves can be neglected in the forward direction because this is the optimal incidence for the boundary algorithm. Second, based on the Huygens–Fresnel principle, we assumed that each point on the boundary acts as a secondary sound source and generates cylindrical waves of the same amplitude in all directions. Third, the scattered waves are not perfectly

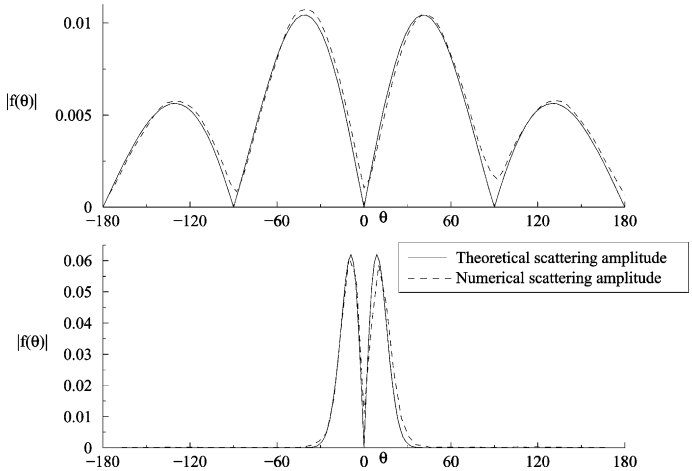

Fig. 23. Comparison between theoretical and numerical scattering amplitude $|f(\theta)|$ in function of θ (in degrees). The mean flow is the Taylor vortex. Top: $\lambda/L_1 = 10$ and $\mathscr{M}_1 \simeq 0.16$. Bottom: $\lambda/L_1 = 1$ and $\mathscr{M}_1 \simeq 0.016$.

cylindrical and one can expect smaller reflection coefficients than previously estimated, especially towards a corner.

- $\lambda/L_1 = 10$: neglecting the distance dependency in f (see Eq. (3)), the maximum amplitude of the scattered wave is $A_s \simeq 0.01A_0$ and is located around $|\theta| = 45^\circ$ (theoretical result from Fig. 23 (top)). Thus, at the north-east corner, the reflected wave amplitude does not exceed at worst $A^{\mathscr{R}} \simeq 0.01 \times 0.4 = 4 \times 10^{-3}$ from the results of the previous tests (Fig. 24). Due to symmetry reasons, this reflected wave produces a new scattered wave with a maximum amplitude at $|\theta'| \simeq 45^\circ$ from its propagation direction, i.e. westward and southward, with a maximum magnitude $A_s^{\mathscr{R}} \simeq 0.01 \times 4 \times 10^{-3} \simeq 4 \times 10^{-5}$. These scattered waves amplitudes are two order of magnitude smaller than the direct scattered wave and can be neglected. Nevertheless, the reflected wave at the north-east corner is just one order of magnitude smaller than the scattered wave and this reflected wave can modify the scattering results. As seen before, in practical situation, these reflected waves do not influence the qualitative and qualitative physical results.
- $\lambda/L_1 = 1$: there is no significant scattering towards the corners so there is no significant reflected waves around the corners. The maximum of the scattering amplitude is then $0.6A_0$ and is located around $|\theta| = 10^\circ$ (theoretical result from Fig. 23 (bottom), please remember that $f \propto \mathscr{M}$). Thus, the upper limit for the reflected amplitude can be estimated to $A^{\mathscr{R}} \simeq 0.6 \times 0.06 = 0.036$. Due to symmetry reasons, this reflected wave produces a new scattered wave with a maximum amplitude at $|\theta'| \simeq 10^\circ$ from its propagation direction, with a maximum magnitude $A_s^{\mathscr{R}} \simeq 0.6 \times 0.036 \simeq 0.02$ (Fig. 25). These waves (reflected and scattered) can be neglected in front of the scattered wave produced by the incident wave-mean flow interactions at the same location.

The above analysis can be conducted for any λ/L_1 ratio and gives an upper bound for the spurious reflection phenomenons. It shows the good behavior of the boundary procedure for sound scattering studies.

Fig. 26 displays the structure of the scattered wave by the Taylor vortex with $\mathscr{M}_1 = 0.16$, for $\lambda/L_1 = 10$ and $\lambda/L_1 = 2$, computed from the numerical results. The observation of the scattered sound field confirms our previous analysis: reflections at the boundary do not alter the results for this scattering problem.

5.2.3. Sensitivity with the domain size

The sound scattering by a Taylor vortex computations have been performed for two different square computational domains of size $l_1 = 0.4$ m (uniform mesh of 512×512 grid points) and $l_2 = 2l_1$, respectively (uniform mesh of 1024×1024 grid points). The acoustic wavelength is $\lambda = 2L_1$ and the Mach number

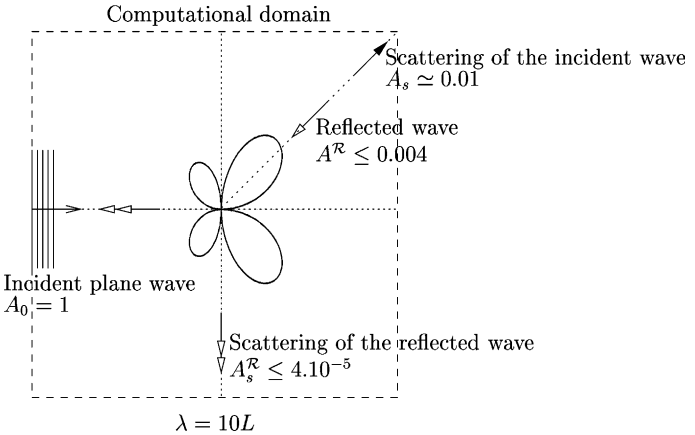

Fig. 24. Order of magnitude of reflected waves for sound-mean flow interaction with $\lambda/L_1 = 10$, in the case of the Taylor vortex with $\mathscr{M}_1 \simeq 0.16$.

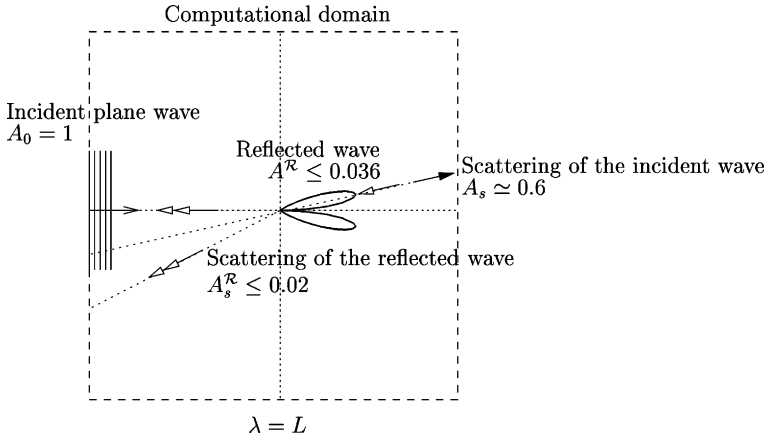

Fig. 25. Order of magnitude of reflected waves for sound-mean flow interaction with $\lambda/L_1 = 1$, with $\mathscr{M}_1 \simeq 0.16$.

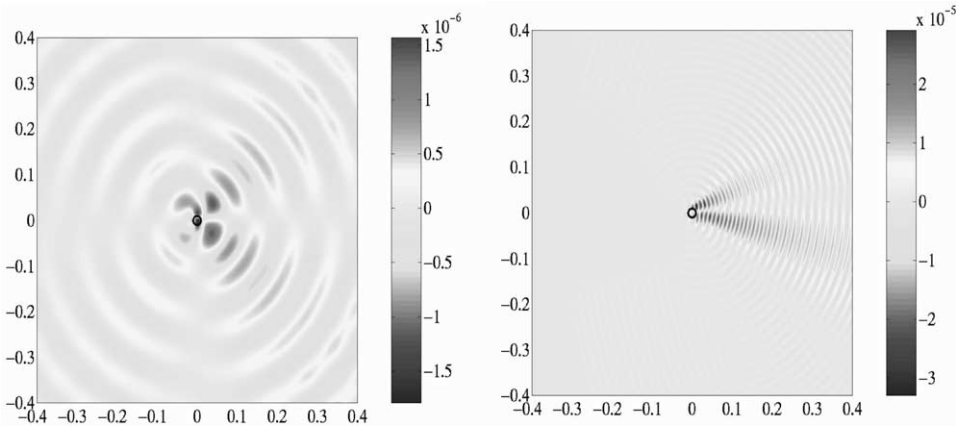

Fig. 26. Numerical scattering density (kg m^{-3}) field for $\lambda/L_1 = 10$ (left) and $\lambda/L_1 = 2$ (right) in the case of the Taylor vortex. The black circle displays the vortex core location. $\mathscr{M}_1 \simeq 0.16$.

is $\mathscr{M}_1 \simeq 0.16$. Fig. 27 shows a comparison of the scattering amplitudes, computed on a circle tangent to the boundaries of the smallest domain, $r = l_1$ (see the scheme on the right of Fig. 27). A very good agreement between the two results is observed, even if the observation distance r is very close to the boundaries of the smallest computational domain. This result confirms the low level of spurious reflections generated by the boundary algorithm and its negligible impact on the scattering results.

5.3. Sound scattering by a vortex pair

The sound scattering by a vortex pair, composed of two Oseen vortices (typical size L_3) of opposite circulation (Fig. 28) has also been considered. This configuration has a great experimental relevance [59] and scattering experiments have been performed using these flows [5,6]. Moreover, it allows a complete description of the sound-mean flow interaction [52]. For a small Mach number, the vorticity of the pair can be modelled by the sum of the vorticity of each vortex

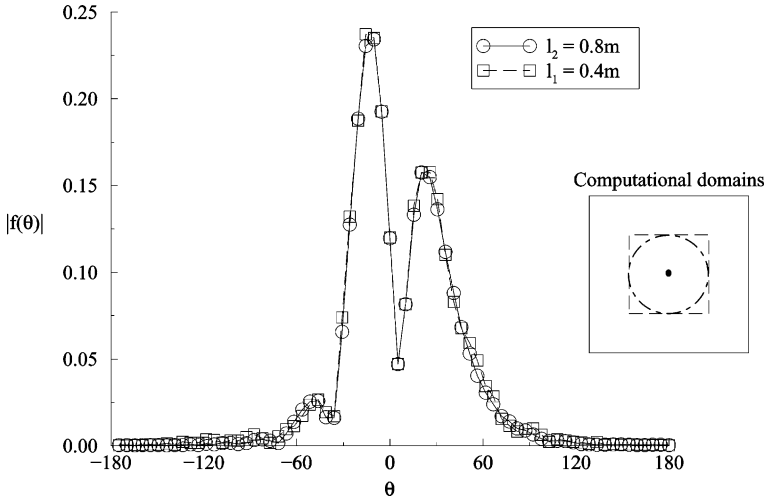

Fig. 27. Comparison of the numerical scattering amplitude $|f(\theta)|$ in function of θ (in degrees) for two domain sizes. The mean flow is the Taylor vortex ($\mathscr{M}_1 \simeq 0.16$), located on the left graph with a black point, and $\lambda/L_1 = 2$. The dashed circle locates the position of the sound recorders.

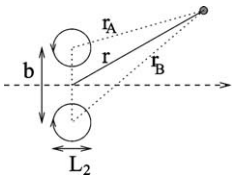

Fig. 28. Schematic configuration for sound scattering by the vortex pair.

$$\overrightarrow{\Omega}_3(r) = \omega_3[\exp(-(r_A/L_3)^2) - \exp(-(r_B/L_3)^2)]\hat{z}, \tag{61}$$

where $L_3 = 0.01$ m, $b = 5L_3 = 0.05$ m and $\rho_{0i} = 2.63 \times 10^{-5}$ kg m^{-3} ($u_{0i} = 10^{-2}$ m s^{-1}). ω_3 is chosen so that the Mach number $\mathscr{M}_3 = 1.26 \times 10^{-3}$. A uniform mesh with 512×512 grid points is used for a domain size $l = 0.4$ m. Fig. 29 shows both the numerical and the theoretical scattering amplitude for $\lambda/L_3 = 2$ (the Born approximation is valid). A good agreement is found despite the unsteadiness of the mean flow due to the vortex pair motion. The advection velocity U_3 of the pair is $U_3 \simeq c\mathscr{M}_3 \simeq 0.38$ m s^{-1}. During the computation, the vortex pair displacement can be estimated to be 1.5×10^{-3} m, which can be neglected in front of the distance of analysis r, so that the theoretical predictions, assuming a steady mean flow, can be used to analyse the numerical results. From a numerical point of view, this motion introduces a new term in the variable $\widehat{V}$ at the boundaries, but this term remains small enough so that condition (34) is still satisfied. Thus, it is still possible to use implementation I_3 in this unsteady situation.

5.4. Three Oseen vortices

A mean flow composed of three Oseen vortices is used to analyse the boundary algorithm behavior for unsteady and high Mach number subsonic mean flows with a global circulation. With this kind of flows, sound scattering exhibits very interesting physical phenomenons such as spirals waves or dislocations [60],

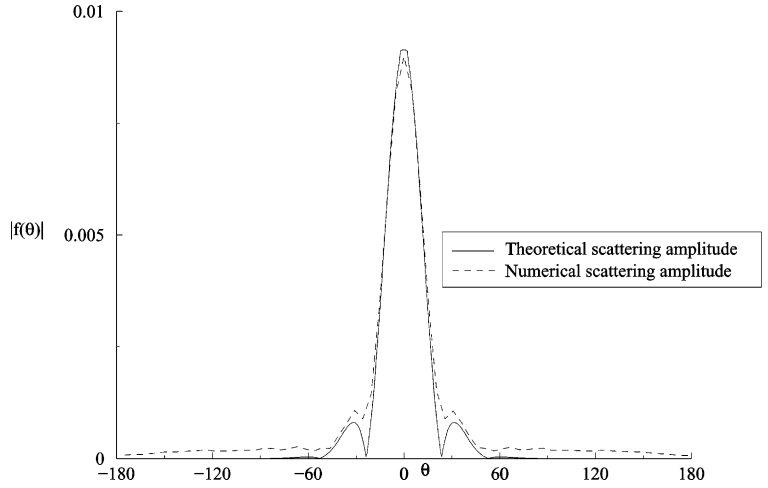

Fig. 29. Comparison between theoretical and numerical scattering amplitude $|f(\theta)|$ in function of θ (in degrees). The mean flow is the vortex pair ($\mathscr{M}_3 \simeq 1.26 \times 10^{-3}$) and $\lambda/L_3 = 2$.

recently observed in experimental surface wave scattering situations [61]. Moreover, this configuration opens the way to the study of sound propagation in disordered vortical flows: the scattering process may become irregular, like in quantum chaos [62,63].

In this configuration, condition (34) may be violated so that implementation I_3 will not be used. Implementation I_1, which proved to be less restrictive in terms of flow topology, is used instead. The three vortices are initially located at the vertices of a equilateral triangle (Fig. 30). They have the same vorticity $\overrightarrow{\Omega}_2$, given by Eq. (48). $L_2 = 0.01$ m and $\omega_2 > 0$ is chosen for each vortex so that the vortices Mach number is $\mathscr{M}_2 \simeq 0.8$. In the computations, the mean flow rotates clockwise. A uniform mesh with 640×640 grid points is used with a domain size $l = 0.5$ m. One can notice that the far-field approximation $r \gg 2\pi L^2/\lambda$,

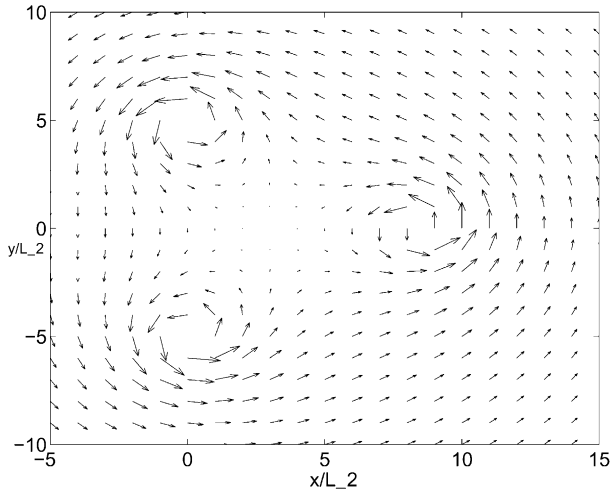

Fig. 30. Initial location of the three Oseen vortices.

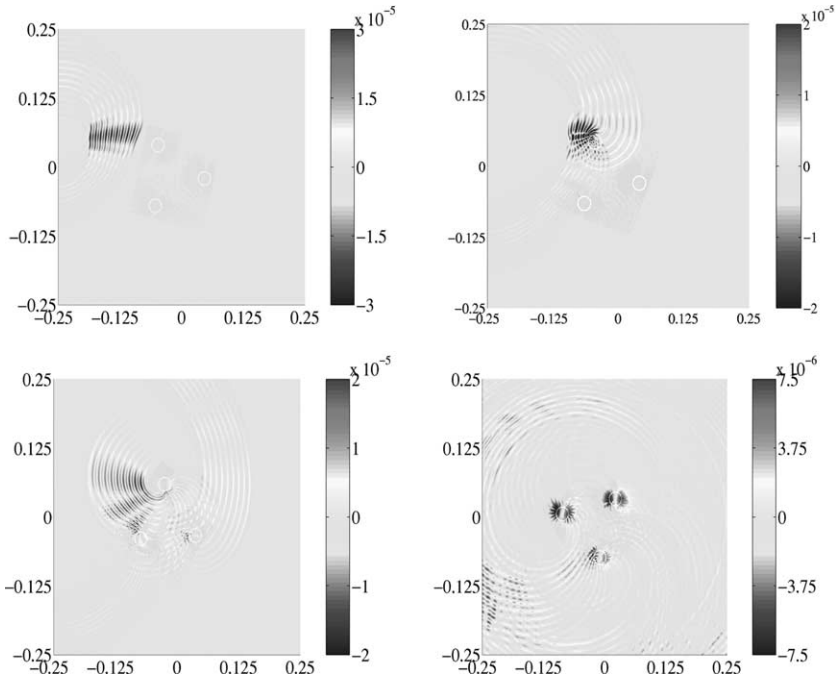

Fig. 31. Sound scattering density (kg m^{-3}) of a pulse by three Oseen vortices ($\mathscr{M}_2 \simeq 0.8$), located at the white circles positions. Left-upper: $t/\mathrm{d}t = 750$, right-upper: $t/\mathrm{d}t = 1000$, left-lower: $t/\mathrm{d}t = 1250$, right-lower: $t/\mathrm{d}t = 2000$.

with L the typical size of the scattering region, is not satisfied in this configuration, even when $r = l/2$, because L is roughly one length of a triangle side $L \simeq 5L_2$ (Fig. 30). A sound pulse (wavelength $\lambda = L_2$) is emitted on the western boundary and propagates through the mean flow. Fig. 31 shows the sound wave density evolution during its interaction with the mean flow: the sound wave is advected by the mean flow and is twisted round the first vortex ($t/dt = 750$ and $t/dt = 1000$). In the same time ($t/dt = 1000$), it is scattered by the same vortex. Later ($t/dt = 1250$), the scattering wave interacts with a second vortex: it is the starting point of a multi-scattering scenario. Nevertheless, in this extreme numerical configuration, the assumptions for implementation I_1 (Eq. (38)) are not fully satisfied and the mean flow does not remain stable at long time: a small advection of the mean flow starts at $t/dt = 1000$ and becomes significant for $t/dt \geqslant 3000$ (not displayed here).

6. Conclusion

A new boundary algorithm for numerical simulations of sound scattering by vortical compressible flows has been introduced. The key point of this algorithm is a decomposition of the physical fields at a given boundary with respect to a steady state which provides a hierarchy of numerical implementations. Then, a Thompson-like approach based on a 1D characteristic method is used to update the fields at the boundaries. Several tests proved the efficiency and allowed a detailed analysis of the algorithm limitations with respect to both the incident sound wave and the mean flow characteristics at the boundary. The algorithm was then used together with a second-order accurate in time and fourth-order accurate in space interior Mac Cormack scheme to simulate sound scattering problems. A good agreement between numerical and

asymptotic theory results was found and an order of magnitude analysis showed that the method is accurate enough for sound scattering problems. Despite some underlying assumptions in the algorithm, a satisfactory behavior for the numerical simulation of unsteady flows with a global circulation and high Mach numbers has also been displayed.

A 2D boundary algorithm [31,43] could be implemented within the proposed framework and might probably give better results. However, we emphasize that the 1D proposed algorithm already gives very good results without any additional filtering operation or buffering zones.

Acknowledgements

We are grateful to Jean-Luc Estivalèzes for providing the interior code and to Stéphan Fauve for stimulating discussions. We thank the referees for helpful suggestions.

Appendix A. Dispersion and damping properties of the interior scheme

The dispersion and damping properties of the interior scheme have been estimated. An incident monochromatic plane wave on the west boundary

$$u_s = u_{0s}\cos(2\pi\nu t) \tag{A.1}$$

propagates along the x direction to the open non-reflecting east boundary. We choose a uniform cartesian grid (128×16 points) with a spatial resolution $\Delta = 7.81 \times 10^{-4}$ m and $u_{0s} = 10^{-2}$ m s^{-1} to ensure a linear behavior. Varying the sound frequency ν, we can compute the acoustical wavelength λ_{num}. Fig. 32 shows the numerical dispersion of the interior scheme: a deviation from the expected non-dispersive behavior of the sound propagation occurs when the number of points per wavelength is less than 12. This deviation remains around 1% even for 8 points per wavelength used. Setting l_x the domain size in the x direction, the damping factor $\tau = \rho_s(x = l_x)/\rho_s(x = 0)$ is plotted versus ν on Fig. 33. If the sound wave is described using more than 25 grid points per wavelength, the numerical damping is very small ($\tau \simeq 1$). It strongly increases when the number of points per wavelength decreases: $\tau = 0.97$ for 13 points and $\tau = 0.87$ for 10 points.

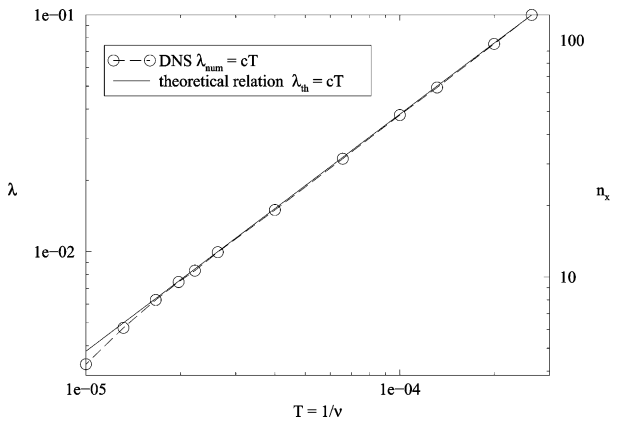

Fig. 32. Numerical dispersion of the interior scheme. Left y axis: wavelength λ. Right y axis: number of grid points n_x.

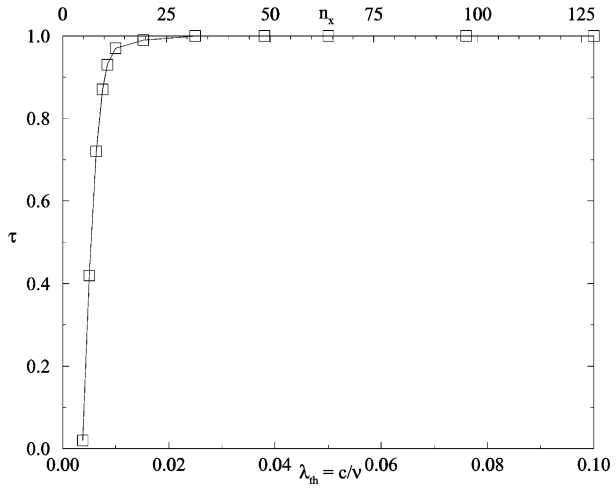

Fig. 33. Numerical damping τ of the interior scheme. Bottom x axis: wavelength λ_{th}. Top x axis: number of grid points n_x.

Thus, a good numerical description of the acoustical properties requires at least 12 points per wavelength with this interior scheme.

References

[1] B. Chu, L.S.G. Kovásznay, Non-linear interactions in a viscous heat-conducting compressible gas, J. Fluid Mech. 3 (1958) 494–514.
[2] A. Ishimaru, Wave Propagation and Scattering in Random Media, Academic Press, New York, 1978.
[3] B. Dernoncourt, J.-F. Pinton, S. Fauve, Experimental study of vorticity filaments in a turbulent swirling flow, Physica D 117 (1998) 181–190.
[4] W. Baerg, W.H. Schwarz, Measurements of the scattering of sound by turbulence, J. Acoust. Soc. Am. 39 (1966) 6.
[5] P.R. Gromov, A.B. Ezerskii, A.L. Fabrikant, Sound scattering by a vortex wake behind a cylinder, Sov. Phys. Acoust. 28 (1982) 6.
[6] C. Baudet, S. Ciliberto, J.-F. Pinton, Spectral analysis of the von Kármán flow using ultrasound scattering, Phys. Rev. Lett. 67 (1991) 2.
[7] K. Oljaca, X. Gu, A. Glezer, M. Baffico, F. Lund, Ultrasound scattering by a swirling jet, Phys. Fluids 10 (4) (1998) 886–898.
[8] R. Labbé, J.-F. Pinton, Propagation of sound through a turbulent vortex, Phys. Rev. Lett. 81 (1998) 7.
[9] S. Manneville, J.H. Robres, A. Maurel, P. Petitjeans, M. Fink, Vortex dynamics investigation using an acoustic technique, Phys. Fluids 11 (11) (1999) 3380–3389.
[10] A.L. Fabrikant, Sound scattering by vortex flows, Sov. Phys. Acoust. 29 (1983) 2.
[11] F. Lund, C. Rojas, Ultrasound as a probe of turbulence, Physica D 37 (1989) 508.
[12] R. Ford, S.G. Llewellyn Smith, Scattering of acoustic waves by a vortex, J. Fluid Mech. 386 (1999) 305, and references therein.
[13] R. Berthet, S. Fauve, R. Labbé, Study of the sound–vortex interaction: direct numerical simulations and experimental results, Eur. Phys. J. B 32 (2003) 237–242.
[14] R.G. Newton, Scattering Theory of Waves and Particles, second ed., Springer, Berlin, 1982.
[15] T. Colonius, S.K. Lele, P. Moin, The scattering of sound waves by a vortex: numerical simulations and analytical solutions, J. Fluid Mech. 260 (1994) 271.
[16] S. Lee, D. Bershader, Head-on parallel blade–vortex interaction, AIAA J. 32 (1994) 1.
[17] B.E. Mitchell, S.K. Lele, P. Moin, Direct computation of the sound from a compressible co-rotating vortex pair, J. Fluid Mech. 285 (1995) 181–202.
[18] L. Gamet, Simulations numériques d'écoulements compressibles. Application à l'aéroacoustique des jets, PhD Thesis, Onera-Toulouse, 1996.

[19] J. Whitmire, S. Sarkar, Validation of acoustic-analogy predictions for sound radiated by turbulence, Phys. Fluids 12 (2) (2000) 381–391.
[20] C. Seror, P. Sagaut, C. Bailly, D. Juvé, On the radiated noise computed by large-eddy simulation, Phys. Fluids 13 (2) (2001) 476–487.
[21] D.J. Lee, S. Ok Koo, Numerical study of sound generation due to a spinning vortex pair, AIAA J. 33 (1995) 1.
[22] C. Bogey, C. Bailly, D. Juvé, Computations of the sound radiated by a 3-D jet using large eddy simulation, AIAA paper 2000-2009 (2000).
[23] S. Candel, Numerical solution of wave scattering problems in the parabolic approximation, J. Fluid Mech. 90 (1979) 465–507.
[24] S. Manneville, P. Roux, M. Tanter, A. Maurel, M. Fink, F. Bottausci, P. Petitjeans, Scattering of sound by a vorticity filament: an experimental and numerical investigation, Phys. Rev. E. 63 (2001) 036607-1.
[25] A. Bayliss, E. Turkel, A far field boundary conditions for compressible flows, J. Comp. Phys. 48 (1982) 182–199.
[26] K.W. Thompson, Time dependent boundary conditions for hyperbolic systems I, J. Comp. Phys. 68 (1987) 1–24.
[27] T.J. Poinsot, S.K. Lele, Boundary conditions for direct simulations of compressible viscous flows, J. Comp. Phys. 101 (1) (1992) 104–129.
[28] C. Hirsh, Numerical Computation of Internal and External Flows, John Wiley & Sons, New York, 1992.
[29] T. Colonius, S.K. Lele, P. Moin, Boundary conditions for direct computation of aerodynamic sound generation, AIAA J. 31 (1993) 9.
[30] S.V. Tsynkov, E. Turkel, S. Abarbanel, External flow computations using global boundary conditions, AIAA J. 34 (1996) 4.
[31] P. Luchini, R. Tognaccini, Direction-adaptive nonreflecting boundary conditions, J. Comp. Phys. 128 (1) (1996) 121–133.
[32] C.W. Rowley, T. Colonius, Discretely nonreflecting boundary conditions for linear hyperbolic systems, J. Comp. Phys. 157 (2000) 500–538.
[33] D. Givoli, Non-reflecting boundary conditions, J. Comp. Phys. 94 (1) (1991) 1–29.
[34] K.W. Thompson, Time dependent boundary conditions for hyperbolic systems II, J. Comp. Phys. 89 (1990) 439–461.
[35] D.H. Rudy, J.C. Strickwerda, A non-reflecting outflow boundary condition for subsonic Navier–Stokes calculations, J. Comp. Phys. 36 (1980) 55–70.
[36] E. Turkel, On the practical use of high-order methods for hyperbolic systems, J. Comp. Phys. 35 (1980) 319–340.
[37] L. Gamet, J.L. Estivalèzes, Non-reflexive boundary conditions applied to jet aeroacoustics, AIAA paper 95-0159 (1995).
[38] S.V. Tsynkov, Numerical solution of problems on unbounded domains, a review, Appl. Numer. Math. 27 (1998) 465–532.
[39] T. Hagstrom, Radiation boundary conditions for the numerical simulation of waves, Acta Numer. (1999) 47–106.
[40] J.B. Keller, D. Givoli, Exact non-reflecting boundary conditions, J. Comp. Phys. 82 (1989) 172–192.
[41] D. Givoli, D. Cohen, Nonreflecting boundary conditions based on Kirchhoff-type formulae, J. Comp. Phys. 117 (1995) 102–113.
[42] B. Engquist, A. Majda, Absorbing boundary conditions for the numerical simulation of waves, Math. Comp. 31 (139) (1977) 629–651.
[43] M.B. Giles, Nonreflecting boundary conditions for Euler equation calculations, AIAA J. 28 (1990) 12.
[44] L. Maestello, A. Bayliss, E. Turkel, On the interaction of sound pulse with the shear layer of an axisymmetric jet, J. Sound Vib. 74 (2) (1981) 281–301.
[45] C.K.W. Tam, Z. Dong, Radiation and outflow boundary conditions for direct computation of acoustic and flow disturbances in a nonuniform mean flow, J. Comput. Acoust. 4 (2) (1996) 1–201.
[46] C. Bogey, C. Bailly, Three-dimensional non-reflective boundary conditions for acoustic simulations: far field formulation and validation test cases, Acta Acoust. 88 (2002) 463–471.
[47] F. Nicoud, Defining wave amplitude in characteristic boundary conditions, J. Comp. Phys. 149 (1999) 418–422.
[48] C. Bogey, C. Bailly, D. Juvé, Numerical simulation of sound generated by vortex pairing in a maxing layer, AIAA J. 38 (12) (2000) 2210–2218.
[49] F.Q. Hu, On absorbing conditions for linearized Euler equations by a perfectly matched layer, J. Comp. Phys. 129 (1996) 201–219.
[50] M.E. Hayder, E. Turkel, Nonreflecting boundary conditions for jet flow computations, AIAA J. 33 (12) (1995) 2264–2270.
[51] H. Atkins, J. Casper, Nonreflective boundary conditions for high-order methods, AIAA J. 32 (3) (1994) 512–518.
[52] R. Berthet, Interaction Son-Écoulement, PhD Thesis, École Normale Supérieure de Lyon, 2001.
[53] G.I. Taylor, On the Dissipation of Eddies, The Scientific Papers of Sir Geoffrey Ingram Taylor, II, Cambridge University Press, Cambridge, 1960, pp. 96–101.
[54] The Oseen vortex is the analogue, for a nonviscous flow, of the burgers vortex, see for example, G.K. Batchelor, An Introduction to Fluid Dynamics, Cambridge University Press, Cambridge, 1994.
[55] R. Vichnevetsky, J.B. Bowles, Fourier analysis of numerical approximations of hyperbolic equations, SIAM Monographs (1982).
[56] L. Landau, E. Lifchitz, Cours de Physique Théorique, Tome 6 (Mécanique des Fluides), deuxième édition, Éditions Mir Moscou, 1989 (Chap. VIII).
[57] P.M. Morse, K.U. Ingard, Theoretical Acoustics, Princeton University Press Edition, Princeton, 1986.
[58] R. Berthet, D. Astruc, S. Fauve, Scattering of sound by vortical flows, in preparation.
[59] T. Leweke, C.H.K. Williamson, Cooperative elliptic instability of a vortex pair, J. Fluid Mech. 360 (1998) 85–119.

[60] M. Umeki, F. Lund, Spirals and dislocations in wave-vortex systems, Fluid Dyn. Res. 21 (1997) 201–210.
[61] F. Vivanco, F. Melo, Surface spiral waves in a filamentary vortex, Phys. Rev. Lett. 85 (10) (2000) 2116–2119.
[62] V. Pagneux, A. Maurel, Irregular scattering of acoustic rays by vortices, Phys. Rev. Lett. 86 (7) (2001) 1199.
[63] R. Berthet, V. Pagneux, A. Maurel, Diffusion irrégulière du son par trois vortex, in: Proceeding of the Sixième Congrès Français d'Acoustique, 8–11 Avril 2002, Lille, France.